CRUSTAL ACCRETION ALONG THE NORTHERN MID ATLANTIC RIDGE (52°-57°N): PRELIMINARY RESULTS FROM EXPEDITION V53 OF *R/V AKADEMIK SERGEY VAVILOV*

Sergey G. Skolotnev*, Alessio Sanfilippo**,✉, Alexander A. Peyve*, Camilla Palmiotto***, Alexander N. Ivanenko°, Marco Cuffaro°°, Ilya A. Veklich°, Filippo Muccini°°,°°°, Ekaterina P. Ponomarenko°, Lorenzo Petracchini°°, Dmitry A. Kuleshov˙, Valentin Basch**, Vitaly N. Dobrolyubov*, Carlotta Ferrando**, Nikolay A. Shkittin*, Camilla Sani**, Tatyana L. Pugacheva˙˙, Manon Bickert˙˙˙, Svetlana A. Dokashenko˙, Yago Nestola***, Elizaveta S. Yakovenko^, Enrico Bonatti***, Pavel A. Gladkich* and Marco Ligi***

   * *Geological Institute, Russian Academy of Sciences, Moscow, Russia.*
 ** *Dipartimento di Scienze della Terra e dell'Ambiente, Università di Pavia, Italy.*
*** *Istituto di Scienze Marine - CNR, Bologna, Italy.*
   ° *Institute of Oceanology, Russian Academy of Sciences, Moscow, Russia.*
  °° *Istituto Geologia Ambientale e Geoingegneria - CNR, Roma, Italy.*
°°° *Istituto Nazionale di Geofisica e Vulcanologia, Roma, Italy.*
   ˙ *Institute of Petroleum Geology and Geophysics SB RAS, Novosibirsk, Russia.*
  ˙˙ *Immanuel Kant Baltic Federal University, Kaliningrad, Russia.*
 ˙˙˙ *Dipartimento di Scienze Chimiche e Geologiche, Università di Modena e Reggio Emilia, Modena, Italy.*
   ^ *Saint-Petersburg State University, Saint-Petersburg, Russia.*
  ✉ *Corresponding author, email: alessio.sanfilippo@unipv.it*

ABSTRACT

This study investigates crustal accretion processes along the northern stretch of the Mid-Atlantic Ridge (MAR) between the Charlie Gibbs (52°-53°N) and Bight (57°N) transforms. These long-lived transform systems, active for more than 40 Ma, bound a ~ 550 km-long MAR segment influenced to the South by the Azores and to the North by the Iceland mantle plumes. The Bight transform is located at the tip of the Reykjanes Ridge, where the spreading direction, influenced by the southward propagation of the Iceland plume, changes from oblique (30° to the axis) to perpendicular to the axis. Four hundred kilometres to the south, the MAR is offset by the Charlie Gibbs transform system consisting of two long-lived right-lateral transform faults linked by a short ~ 40 km-long spreading segment. Previous expeditions surveyed large areas of these two transform systems, defining their main morphological features. Based on these bathymetric data, Expedition V53 of the *R/V A.S. Vavilov* carried out an intense dredging program coupled with magnetic surveys in an area spanning from 57° to 52°N, covering both the Bight and the Charlie Gibbs transform systems. We collected 1850 kg of rock samples including limestones, basalts, gabbros and mantle peridotites from 27 dredging sites, along with two 6-m long sedimentary cores. The sampled lithologies are globally in agreement with the contrasting morphological features of the two transform faults. We discuss here and compare the geology of these two major transform systems and assess the influence of the Icelandic plume on seafloor morphology at the Bight Fracture Zone.

INTRODUCTION

The stretch of the Mid-Atlantic Ridge (MAR), south of Iceland and north of Azores, is affected by two mantle plumes centred on Iceland and Azores, respectively. These plumes play an important role on mantle dynamics beneath the MAR axis and, together with plate kinematics, have been influencing the geodynamic evolution of the entire North Atlantic MAR system for the last ~ 34 Ma (Vogt et al., 1971; Vogt and Avery, 1974; Hey et al., 2016; Ligi et al., 2022). Local variations in mantle composition and temperature have a major control on mantle melting and magmatism that, consequently, drive different modes of crustal accretion (e.g., Cannat et al, 2006; Escartin et al., 2008; Tucholke et al., 2008; Schouten et al., 2010; Olive et al., 2010). In addition, spreading reorganization can result from a thermally induced change in lithospheric behaviour occurring when plume head isotherm progressively interacts with pre-existing ridge segments (White, 1997; Jones, 2003; Hey et al., 2010). This process may progressively eliminate transform faults and lead to a reorganization of the pre-existing ridge geometry,

as observed at the Reykjanes Ridge (e.g., Martinez and Hey, 2022).

The North MAR axis between the Azores and Iceland is displaced by two major transform zones at ~ 57°N and ~ 52°N, the Bight and Charlie Gibbs, respectively (Fig. 1). These two first order discontinuities mark a potential boundary between different mantle domains, whose properties may control the large-scale evolution of the North Atlantic Ocean (e.g., Blichert-Toft et al., 2005; Martinez et al., 2020).

The Bight transform, located at 56.8°N at the tip of Reykjanes Ridge (Fig. 1), is the northernmost remaining active transform fault offsetting the MAR south of Iceland. Between the Modred Non-Transform Offset (NTO) and Iceland, the Reykjanes Ridge is a continuous ~ 30° oblique ridge axis showing no transform displacements (Fig. 1; Hey et al., 2016; Martinez and Hey. 2022). This indicates that the active transform-eliminating reorganization tip of the Icelandic plume is currently located at the Modred NTO (56.9°N; Martinez et al., 2020).

A detailed bathymetric and magnetic survey recently carried out south of the Modred NTO allowed to reconstruct the

position and evolution of the ridge segment during recent geological times (Benediktsdóttir et al., 2016). Results suggest that the ridge segment south of the Modred NTO is presently being reoriented under the influence of the southernmost flow of the Iceland plume (Fig. 2). Yet, geodynamic reconstructions indicate that the reorganization of Reykjanes Ridge has no direct influence on the MAR south of the Bight transform (Benediktsdóttir et al., 2016; Hey et al., 2016; Skolotnev et al., 2022). This segment is characterized by an orthogonal spreading direction; several ridge propagating events have been identified based on magnetic anomalies asymmetry (Benediktsdóttir et al., 2016). Complex interaction between the Reykjanes Ridge north of the Bight Transform Zone and the MAR to the south led to the reorganization of the ridge dynamics in the immediate vicinity of the transform fault. As a result, the active spreading segment south of the Bight transform has undergone two relatively large relocations toward the East (9 km and 6 km) within the past 1 Ma (Fig. 2), in turn shortening the offset of the Bight transform fault (Benediktsdóttir et al., 2012; Hey et al., 2016).
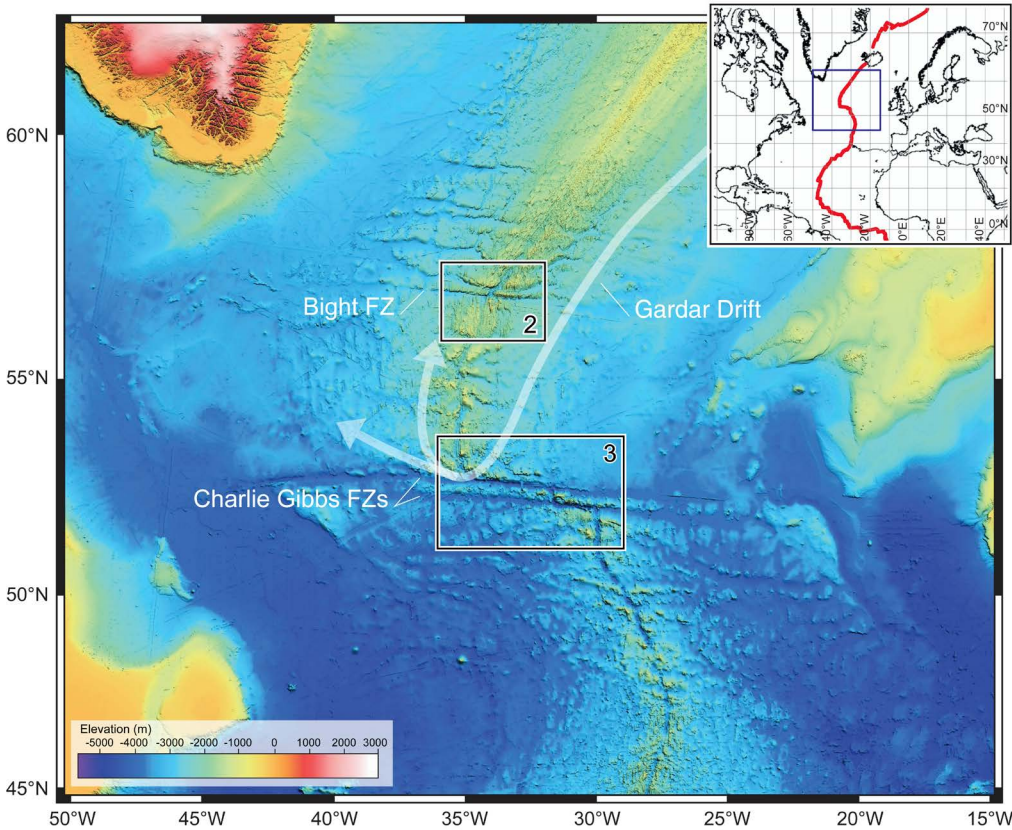

Fig. 1 - Bathymetry of the northern Mid-Atlantic Ridge from the GEBCO_2022 Grid (GEBCO Compilation Group 2022, doi:10.5285/e0f0bb80-ab44-2739-e053-6c86abc0289c). Location of the Bight and Charlie Gibbs Fracture Zones are indicated. Numbered white boxes indicate Figs. 2 and 3 in this paper, each with bathymetry of specific areas. The inset in the top right corner shows the location of the studied area along the Mid-Atlantic Ridge. White arrows represent Iceland-Scotland Overflow Water.
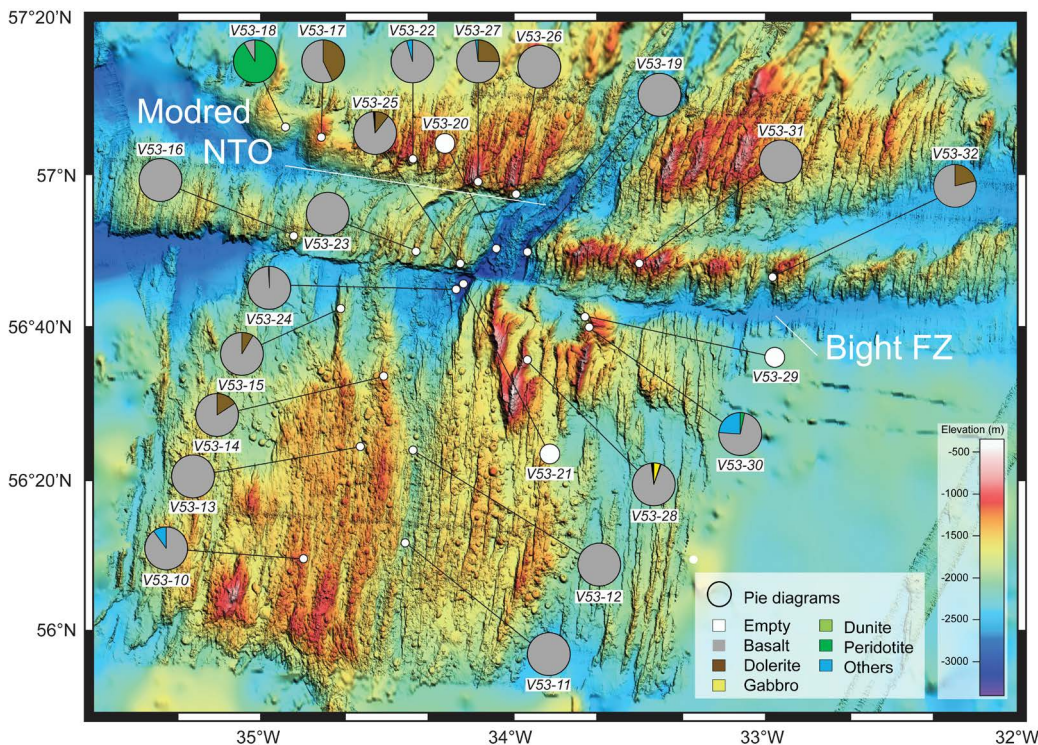

Fig. 2 - Shaded-relief morpho-structural image of the Bight transform and Modred NTO, together with locations of dredging stations. The multibeam bathymetry of the R/V Marcus G. Langseth expedition in 2013 (Hey et al., 2016) is superimposed to GEBCO_2022 grid (GEBCO Compilation Group 2022, doi:10.5285/e0f0bb80-ab44-2739-e053-6c86abc0289c). Dredging stations are indicated by white circles while the lithology of the collected rocks is represented by pie charts showing the proportion of lithologies recovered.

Moving south, the Charlie Gibbs transform system is located between 52.1°N and 52.7°N (Fig. 3). This system offsets the MAR axis by about 340 km and is formed by two distinct transform faults linked by a short ~ 40 km-long spreading segment (e.g., Johnson, 1967; Fleming et al., 1970; Searle, 1981; Calvert and Whitmarsh, 1986; Whitmarsh and Calvert, 1986; Skolotnev et al., 2021). The Charlie Gibbs region was investigated mostly by geophysical surveys during the '70s (Fleming et al., 1970; Vogt and Avery, 1974; Lonsdale and Shor, 1979; Searle, 1981) but also sampled and mapped in more details during later expeditions (Smoot and Sharman, 1985; Whitmarsh and Calvert, 1986; Hekinian and Aumento, 1973; Sigurdsson, 1981; Shilling et al., 1983; Chernysheva and Kharin, 2009).

More recently, Expeditions CE15007, CE16014, CE18008 with the *R/V Celtic Explorer* (Georgiopoulou and CE18008 Scientific Party, 2018) and Expedition S50 with the *R/V A.N. Strakhov* conducted detailed bathymetric surveys of the entire Fracture Zone, including the adjacent southern and northern MAR segments (Fig. 3; Skolotnev et al., 2021). The new surveys show the widespread occurrence of corrugated surfaces exposing lower crust and mantle material, also called "megamullions" or oceanic core complexes (OCCs). These structures are mainly located in the domain bordered by the two fracture zones, on both sides of the intra-transform spreading axis. The widespread occurrence of OCCs indicates that crustal accretion at the intra-transform spreading segment (ITR) is mainly driven by tectonic processes associated to lower crustal exhumation, with no evidence of long-lived magmatic activity typical of a volcanic seafloor (Skolotnev et al., 2021).

In this study, we present new data collected during cruise V53 with the *R/V Akademik Sergey Vavilov* in September and October 2021. Based on existing bathymetric data, we here provide a comprehensive view of the rocks exposed in the vicinity of the Bight Fracture Zone (FZ), including dome-shaped structures located along the northern wall of the Modred NTO and reliefs east of the present-day spreading axis south-east of the Bight active transform fault. Basalts of different ages sampled along single flow lines will provide a temporal evolution of the magmatism in the area.

Our new sampling is of particular interest considering the lack of samples reported to date in the Bight FZ. In addition, we provide here a more complete view of the lithologies exposed in the Charlie Gibbs FZ, covering several gaps of the last sampling cruises. Our new data also include a geophysi-
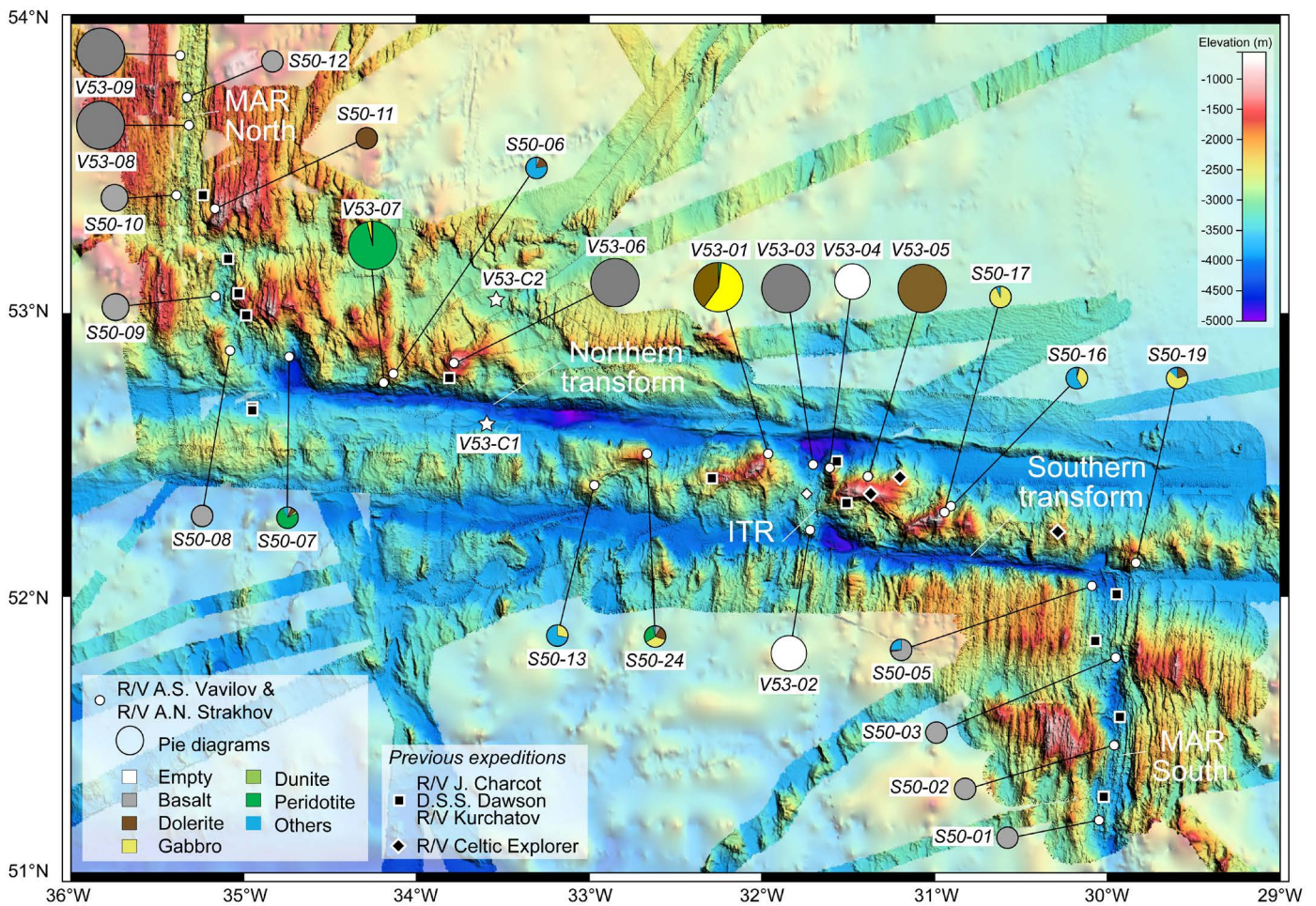

Fig. 3 - Bathymetry of the Charlie Gibbs transform system and location of dredging stations. Bathymetric map results from a compilation of several multibeam datasets including our own from cruise S50 (Skolotnev et al., 2021), and those from the recent expeditions of the R/V Celtic Explorer (Georgiopoulou and CE18008 Scientific Party, 2018; Georgiopoulou and Murton, 2018; Marine Institute of Ireland, AORA Bathymetry database: https://erddap.marine.ie/erddap/griddap/AORA_asc.html; Furey, 2020). The light bathymetry in background is from the GEBCO 2021 15-arcsec global grid (doi:10.5285/c6612cbe-50b3-0cff-e053-6c86abc09f8f). Dredge stations from ours (S50 and V53) and previous expeditions of the R/V Jean Charcot (Hekinian and Aumento, 1973), R/V C.S.S. Dawson (Hekinian and Aumento, 1973; Sigurdsson, 1981; Shilling et al., 1983), R/V Kurchatov (Chernysheva and Kharin, 2009). Note that the large OCC within the ITR has been extensively sampled during the recent expeditions of the R/V Celtic Explorer.

cal survey that acquired high-resolution magnetic profiles in the Bight FZ. These new data are used here to compare the large-scale structure and the geodynamic evolution of these transform domains, with detailed petrological characterizations and geodynamic reconstructions.

GEOLOGICAL SETTING

Bight transform

The Bight transform offsets by 15 km eastward the MAR at 56°47'N. It is a left-lateral transform separating the Mid-Atlantic from the Reykjanes Ridge (Fig. 2), and is considered as a long-lived transform despite its short offset (Müller and Roest, 1992; Benediktsdóttir et al., 2016 and reference therein). Recent geophysical surveys have provided high-resolution descriptions of its morphology (Hey et al., 2016) and magnetic pattern (Benediktsdóttir et al., 2016). The Bight Fracture Zone is characterized by a complex tectonic domain, which coupled to the Modred NTO separates orthogonal spreading along the MAR in the southern area from the 30°-oblique spreading kinematics along the Reykjanes Ridge in the northern region (see Hey et al., 2016; Martinez et al., 2020; Martinez and Hey, 2022). The geodynamic evolution of this stretch of MAR is still debated; south of the Modred NTO, the ridge segment is presently being reoriented under the influence of the southernmost flow of Iceland plume (Benediktsdóttir et al., 2016; Martinez et al., 2020). Conversely, based on high-resolution bathymetric data, Hey et al., (2016) proposed that the V-shaped ridges related to the Reykjanes Ridge southward propagation do not extend south of the Bight transform (Benediktsdóttir et al., 2016).

A detailed magnetic survey by Benediktsdóttir et al. (2016) across the MAR segment south of the Bight transform shows asymmetries in spreading geometries interpreted as due to repeated rift propagation events (e.g., Bruguier et al., 2003; Benediktsdóttir et al., 2016). Benediktsdóttir et al. (2016) identified 12 rift propagation events in the area, which imply a complex ridge reorganization during the last 6 Ma. These authors conclude with great confidence that in the last 4 Ma most of the identified propagators transfer the lithosphere from Eurasia to the North American plate. Consistently, they deduce that in recent times (< 1 Ma), the spreading segment south of the Bight transform has been relocated ~ 15 km eastward (Benediktsdóttir et al., 2016; Hey et al., 2016).

Most MAR segments immediately south and north of the Bight transform display low to moderate levels of seismic activity if compared to other active segments of the MAR (Fig. 4). Earthquake parameters occurring from January 2000 to October 2019 from the International Seismological Centre (ISC, On-line Bulletin, https://doi.org/10.31905/D808B830) and from the global Centroid Moment Tensor (CMT, www.globalcmt.org) catalogue report that only 19 events with magnitude $M_w \geq 5$ occurred in the region during the last 20 years. The largest earthquake ($M_w = 5.6$) took place on September 10th, 2017, in the vicinity of the southern tip of the Reykjanes Ridge. The MAR segment south of the Bight transform and away from the ridge-transform intersection lacks seismicity, whereas the Reykjanes Ridge segment to the north is dominated by a large number of earthquakes with low to moderate magnitudes (Fig. 4). Focal mechanisms from the global Centroid Moment Tensor (CMT) catalogue show a normal dip-slip on approximately N-S MAR trending faults with a focal depth ranging from 5 to 19 km, suggesting the proximity of the brittle-ductile transition close to these depths.
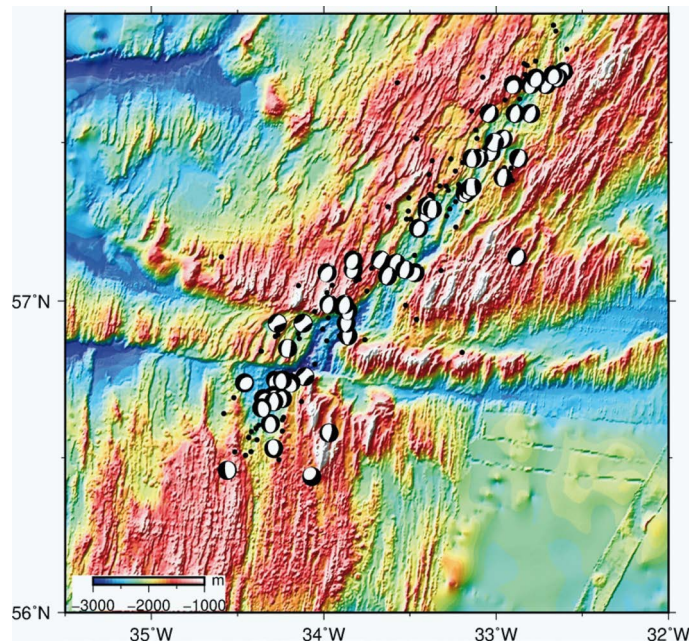

Fig. 4 - Seismicity of the Bight transform region from the International Seismological Centre Event catalogue (www.isc.ac.uk). Focal mechanisms (beach balls) are from the Centroid Moment Tensor (CMT) catalogue (www.globalcmt.org). Fault plane solutions show prevalent E-W extension along the northern Mid Atlantic Ridge segments, with centroid depths ranging from 5 to 19 km.

Charlie Gibbs transform

The Charlie Gibbs transform system is formed by two narrow sub-parallel right-lateral transform faults (Johnson, 1967; Fleming et al., 1970) offsetting by 340 km two long MAR stretches and including, in the intra-transform region, a ~ 40 km-long spreading segment (ITR) centred at ~ 52.5° N and ~ 31.5° W (Fig. 3). Their fracture zones oriented E-W dissect the entire North Atlantic oceanic seafloor, suggesting that the two transforms were active since the early rifting stage between Europe and North American plates (e.g., Johnson et al., 1971; Olivet et al., 1970; 1974; Roberts et al., 1979). In addition, some authors suggested a possible landward extension within the continental margin up to the intersection with the Dover Fault in Newfoundland (Haworth, 1977).

The ~ 110 km-long southern transform consists of a single narrow strike-slip zone following the small circle path of the pole of rotation (Searle, 1981) and trending 95° N (Fig. 3). The active part of the transform valley is free of sediments, whereas the sedimentary cover appears to increase to the east in the inactive valley. In contrast, the ~ 230 km-long northern transform has a thick sedimentary infill and a 20 km-wide active transform valley that masks most of the basement structures (Searle, 1981). Large magnitude earthquakes occur along the northern transform, with random locations along the transform valley and a wide distribution of the seismic swarm events (Kanamori and Stewart, 1976; Bergman and Solomon, 1988; Aderhold and Abercrombie, 2016). The most significant events occurred in 1974 and 2015, with magnitudes M_w 6.9 and M_W 7.1, respectively (Aderhold and Abercrombie, 2016).

The axial part of the ITR has been investigated in detail by CE15, CE16014 and CE18008 Irish expeditions with the

R/V Celtic Explorer, which first postulated the occurrence of core complexes exhumed by low angle normal faults (Georgiopoulou and Murton, 2018). Results from these expeditions show that the oceanic crust becomes thinner toward the ridge-transform intersection, reaching a thickness of 3.5 km within the intra-transform domain (Whitmarsh and Calvert, 1986; Calvert and Whitmarsh, 1986), which is consistent with studies on large transforms elsewhere (e.g., Prince and Forsyth, 1988; Bonatti et al., 1996; Ligi et al., 2005). More recently, Skolotnev et al. (2021) showed that this 40 km-wide intra-transform domain formed at the ITR is characterized by successive large dome-shaped bathymetric highs irregularly distributed either on the northern wall of the southern transform valley or on the southern wall of the northern transform valley (Fig. 3). Based on the occurrence of well-developed spreading-parallel corrugations and the exposure of lower crustal and mantle lithologies, Skolotnev et al. (2021) interpreted all these dome-shaped structures as OCCs formed by long-lived detachment faulting (e.g., Escartin et al., 2008; MacLeod et al., 2009). The largest OCC, located on the eastern side of the ITR, has been recently mapped and sampled by ROV dives during expedition CE18008 (*R/V Celtic Explorer,* see Georgiopoulou and Murton, 2018; Georgiopoulou and CE18008 Scientific Party, 2018), whereas other two OCCs east and west of the ITR were mapped and sampled during Strakhov 50 Expedition (Skolotnev et al., 2021; 2022). Dredge hauls deployed on the dome-shaped structures recovered gabbros, peridotites and, locally, dolerites, further confirming the occurrence of detachment surfaces (Fig. 3). The widespread occurrence of OCC indicates that the crustal accretion in the ITR was driven by tectonic spreading, mainly accommodated by faulting and lower crustal exhumation, with no evidence of long-lived magmatic activity typical of volcanic seafloor. In addition, Skolotnev et al. (2021) noted two principal dipping directions for the detachment surfaces of the OCCs, which suggest a cyclic formation of OCCs during lithospheric accretion within the short ITR segment.

The architecture of MAR segments located north and south of Charlie Gibbs (MAR North and MAR South, respectively; Fig. 3) is characterized by well-developed volcanic fabrics indicative of intense and continuous magmatic activity. Nonetheless, the two MAR segments show different morphologies when approaching the transform zone: MAR South is characterized by a regular topography, with abyssal hills oriented perpendicular to the spreading direction. Fresh basalt glasses were sampled along-axis and within the nodal basin (see Fig. 3; Skolotnev et al., 2021). In contrast, the MAR North segment reveals a gradual transition from regular abyssal hill fabric in the north related to a robust magmatism, to morphologies related to a highly segmented spreading axis as the ridge approaches the transform fault, in the south. There, Skolotnev et al. (2021) described a dome-shaped structure at ~ 34ºW with exposure of lower crustal and mantle rocks in the vicinity of the ridge-transform intersection (RTI), interpreted as an OCC exhumed by detachment faulting. The architecture of the seafloor in this sector can thereby be related to tectonic denudation due to a decreas

Basalt chemistry

Fig. 5 compares chemistry of basaltic glasses and depth of the MAR axis between 50ºN and 58ºN (data from the Petrological Database of the Ocean Floor, PETDB). The regional-scale variability indicates differences in Na_8 contents (i.e., Na

contents normalized to MgO = 8 wt%; Klein and Langmuir, 1987) and La_N/Sm_N ratios at the Charlie Gibbs transform system. Here, variations in regional topography are correlated to a sudden change in basalt chemistry as suggested by Na_8 and La_N/Sm_N contents (Fig. 5). South of the Charlie Gibbs transform, basalts are characterized by higher Na_8 and higher La_N/Sm_N ratios relative to those from the northern portion (Fig 5b and c). Notably, the highest Na_8 values and La_N/Sm_N ratios are from few basalts sampled off-axis in the intra-transform domain. Such variations in basalt chemistry indicate higher degrees of melting and mantle temperatures in the northern MAR sector than in the ITR and in the southern MAR sectors (e.g., Schilling et al., 1993; Blichert-Toft et al., 2005; Skolotnev et al., 2021).

Some further inference can be drawn by examining the covariation in isotope ratios along the ridge axis of the different MAR sectors. South of 50ºN and north of 60ºN (not shown in Fig. 5), melts show gradually more enriched isotopic compositions, i.e., increase in $^{87}Sr/^{86}Sr$ (Fig. 5d) and $^{206}Pb/^{204}Pb$ (Fig. 5f) coupled with a decrease in $^{143}Nd/^{144}Nd$ (Fig. 5e) and $^{176}Hf/^{177}Hf$, resulting from the influence of the Azores and Iceland mantle plumes, respectively (see a review in Shilling et al., 1993 and Blichert-Toft et al., 2005). North
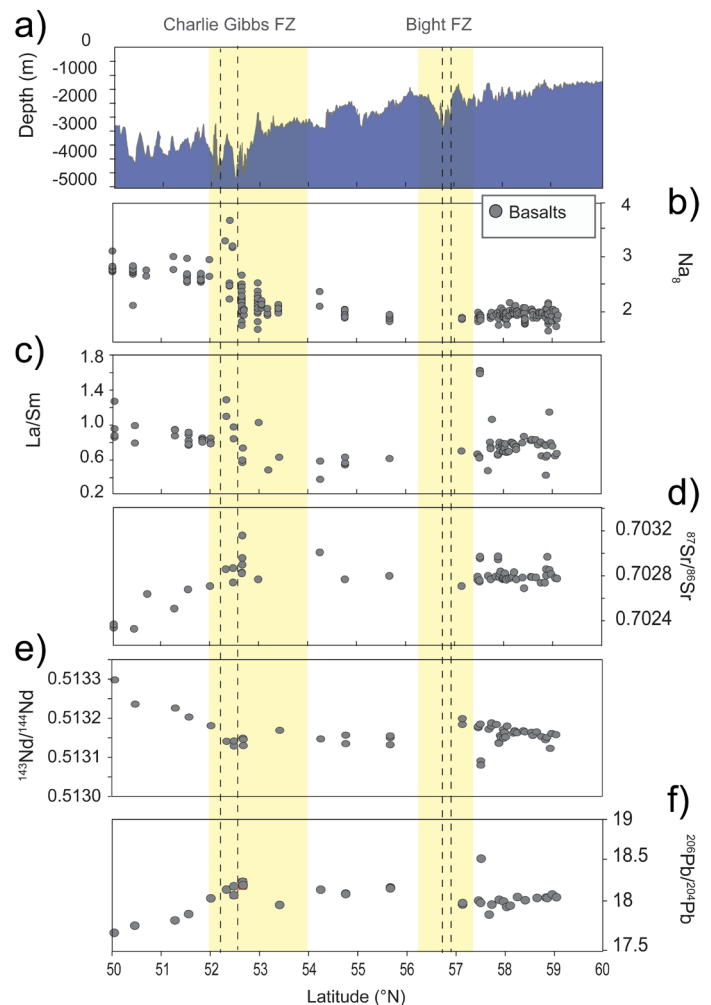

Fig. 5 - Axial depth profile (a) and along-axis variations of basalt glasses in (b) Na_8, (c) La_N/Sm_N, (d) $^{87}Sr/^{86}Sr$, (e) $^{143}Nd/^{144}Nd$ and (f) $^{206}Pb/^{204}Pb$ (data compiled from PetDB_Database, www.earthchem.org/petdb). Normalization values are after Sun and McDonough (1989).

of 50°N, variations in axial depths are mirrored by variations in radiogenic isotopes, which become gradually more radiogenic in Pb and Sr, and less radiogenic in Nd and Hf isotopes approaching the Charlie Gibbs FZ to the north (Schilling et al., 1993; Blichert-Toft et al., 2005). From the Charlie Gibbs to the Bight FZ, basalt isotopic compositions are rather homogeneous (Fig. 5). Within the Charlie Gibbs intra-transform domain, however, the few available data are restricted to off-axis magmatism and the current spatial distribution of samples analyzed north and south of the transform system is too limited to invoke the existence of a change in mantle composition corresponding to this long-lived axial discontinuity.

A detailed analysis of basalt chemistry variability across the Bight FZ is hampered by the lack of available geochemical data on basalt glasses from 55.6°N to 57.1°N. However, as documented at the Charlie Gibbs FZ, the geochemistry of the few basalts recovered in the vicinity of the Bight transform suggests a decrease in Pb[206], Pb[207], Nd and Hf isotope compositions, potentially in correspondence with the Bight discontinuity. Hence, although the scant literature data seem to reveal a possible link between mantle composition, mantle temperature and evolution of these major fracture zones, this hypothesis is still not confirmed due to a lack of available samples. Therefore, the extent to which segmentation in this sector of the MAR is influenced by the combined effect of the Azores and Iceland mantle plumes is still a matter of debate.

EXPEDITION V53 (*R/V A. S. Vavilov*)

Material and methods

Bathymetric data

Multibeam data of the Bight Fracture Zone are available from the NGDC Bathymetry Database. They were collected by a hull-mounted Kongsberg EM122 1°x1° 12 kHz multibeam echo-sounder with *R/V Marcus G. Langseth* in 2013 (Hey et al., 2016). Retrieved raw multibeam data were processed using the Kongsberg NEPTUNE software encompassing statistical and geometrical (angle and distance) filters to remove coherent and incoherent noise in each swath, together with manual removal of spikes due to single fake soundings. Spatial analysis and mapping were performed using GMT (Wessel and Smith, 2006) and PLOTMAP (Ligi and Bortoluzzi, 1989) packages. Multibeam data were gridded to produce a high-resolution bathymetric grid with cell-size of 50 m. In addition, during the cruise, bathymetric data have been acquired using a single beam hydrographic Kongsberg EA600 echo sounder in order to show details of seafloor morphology during dredging and magnetic profiling.

Magnetics

Magnetic data were collected using a Marine Magnetics SeaSpy II magnetometer towed 220 m behind the stern to reduce the field induced by the vessel. The towing system consists of a vectran cable with twisted pair conductors. The SeaSpy uses the Overhauser effect based on the measurement of the magnetic flux density. The sensor sensitivity is 0.01 nT and it is externally triggered by a RS232 protocol interfaced with a dedicated notebook. Data were recorded by the Marine Magnetics's Sealink software at 1 Hz sampling rate (equivalent to an average acquisition point distance of about 3 m). Positioning was assured by the NMEA sentences provided by the GPS antenna of the ship. About 2500 km of magnetic profiles were acquired across the MAR axis in the Charlie Gibbs and Bight regions.

Gravity

Available gravity data from the Bight transform area were analyzed before the expedition for better cruise planning. Free air gravity values (Fig. 6a) were obtained from the satellite derived gravity grid (version 30) of Sandwell et al. (2014). The contributions to the gravity field of variations in crustal thickness or crustal and upper mantle density anomalies have been calculated removing the predictable signals produced by density contrast between water and rock at the seafloor, and by density variations associated with the temperature field following the method detailed in Ligi et al. (2022). The mantle Bouguer correction was obtained by replacing the water layer (density of 1040 kg/m^3) and an 8 km constant thickness crust (density of 2690 kg/m^3) limited by and parallel to the top of the basement topography, with a layer of mantle material (density of 3330 kg/m^3). The crustal interface attraction predicted values, computed at bathymetry grid points, were interpolated onto the satellite gravity grid points, then subtracted from the corresponding free air anomalies. The new values were then re-gridded at 0.5 km to obtain the complete mantle Bouguer anomaly (MBA) shown in Fig. 6b with an arbitrary zero level corresponding to the centre of the range in anomaly amplitudes.

Mantle temperatures were estimated to predict gravity anomalies due to density variations caused by the mantle thermal structure by solving the steady-state advection-diffusion heat equation over a three-dimensional domain of mantle flow calculations (Fig. 7), assuming 0°C at the seafloor and 1350°C at 150 km of depth and a variable grid spacing (2048 x 1024 x 101) with highest grid resolution at the plate boundaries (Morgan and Forsyth, 1988). Density changes due to temperature assuming a thermal expansion coefficient of 2.75 10^{-5}/°C, chosen to match an averaged MBA profile, in a least square sense, along a 10 km wide corridor centred on a flow-line from the midpoint of the MAR segment south the Bight transform (profile B-B' of Fig. 6a). Mantle flow velocities were estimated assuming steady-state plate-thickening passive flow (Ligi et al., 2008). The predicted thermal mantle contribution (TMGA) was then subtracted from the MBA (Fig. 6a) to create the residual anomalies (RMBA). The computed residual low-pass filtered mantle Bouguer anomalies, (wavelengths shorter than 22 km were cut off), were downward continued to a depth of 10 km below sea-level, to infer crustal thickness variations, assuming a crust-mantle density contrast of 640 kg/m^3.

Dredging

Seafloor sampling was performed with cylindrical dredges; a total of 32 dredges were deployed, of which 5 were empty and 2 lost. Most of the empty dredges were in the ITR valley of the Charlie Gibbs transform system and at the ridge axis displaced by the Bight transform (Figs. 2 and 3). During Expedition V53, ~ 1850 kilograms of rocks were collected in 27 dredges deployed in the two study areas (Table 1 and Figs. 2 and 3). We divided the recovered rock samples by lithology and defined the initial rock proportions based on primary minerals. Secondary minerals and alteration intensities were also defined for each sample and reported separately. Mineral modal compositions, the extent of alteration, crystal-plastic and brittle deformation intensities were defined macroscopically on board the *R/V A.S. Vavilov*, following the methods used during Expedition S45 and S50 (Skolotnev et al., 2020; 2021). Crystal-plastic deformation intensity in peridotites and gabbros was quantified based on foliation, grain size, and relative proportions of neoblasts. Offshore microscopic anal-
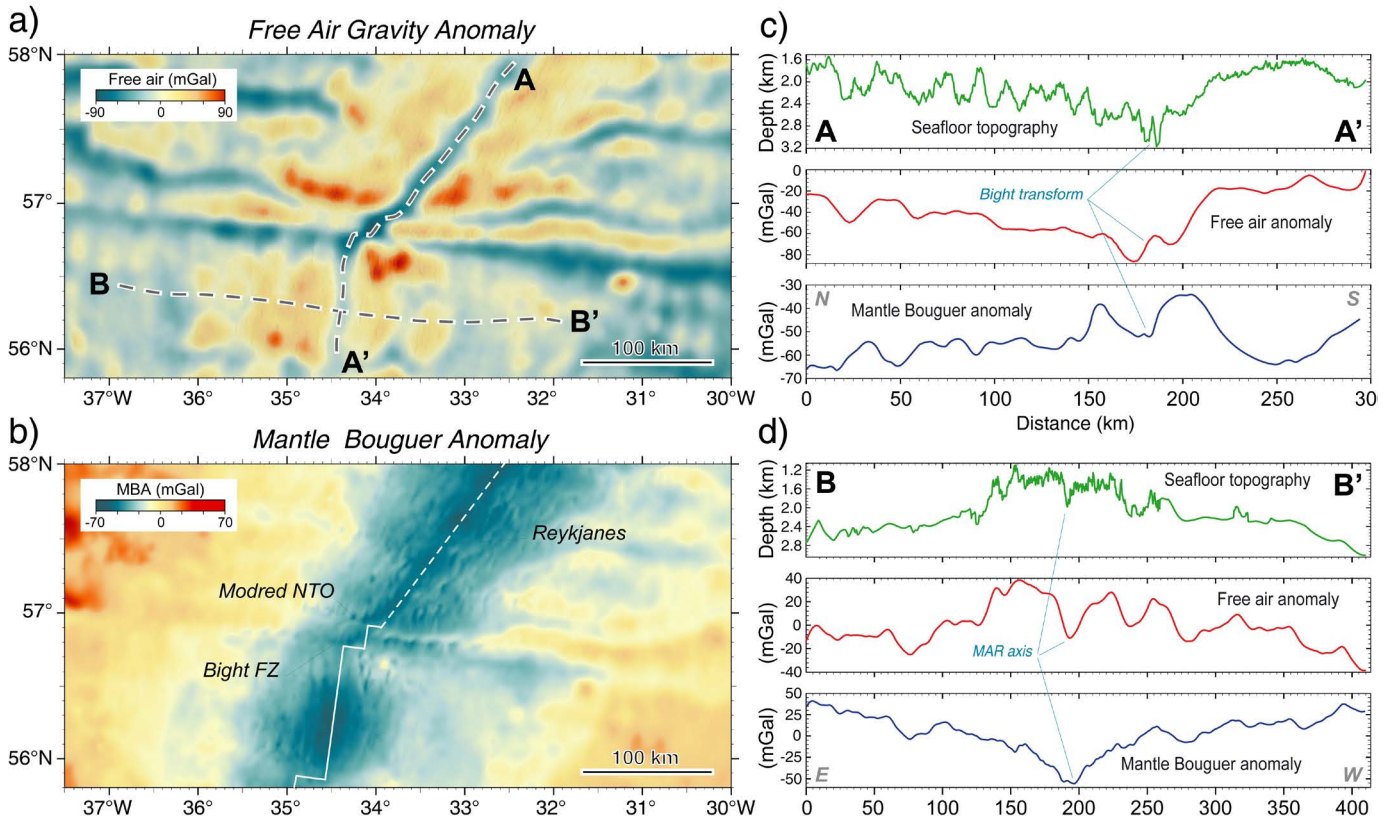
Fig. 6 - Gravity anomalies of the southern end of the Reykjanes Ridge and Bight transform. a) Free air anomalies; b) Mantle Bouguer anomalies. Topography (top), free air gravity anomaly (middle) and mantle Bouguer anomaly (bottom) along selected profiles: c) along-axis zero-age section A-A'; and d) southern MAR flow-line section B-B'.

yses of representative samples followed the shipboard observations to test the accuracy of the definition of rock types and deformation intensity. Coherence between dredging hauls was ensured by each member of the petrological team being responsible of a specific aspect of the description (i.e., rock type, textures, mineral modes, and habits). Sedimentary rocks were described based on the nature of the matrix and the variability of clasts: monomictic breccia with basalt pillow clasts and hyaloclastite were included as 'basalts' for the total quantification of rock-type, while polymictic breccia and carbonates were considered separately. The occurrence and mineralogy of veins, iron-manganese coating and secondary alteration of glass was also reported.

Coring

Two sediment cores were taken in the Charlie Gibbs transform domain using a 6 m long gravity corer with inner diameter of 11 cm. The sampling sites were chosen based on acoustic profiling acquired in cruise S50 of the *R/V Akademik Nikolaj Strakhov* (Skolotnev et al., 2021). A 465 cm long sediment core V53-C1 was recovered at the top of the channel-related contourite drift at 3851 m water depth (52°37.080'N; 33°34.726'W), on the southern flank of the Charlie Gibbs northern transform valley (Fig. 3). Sediment
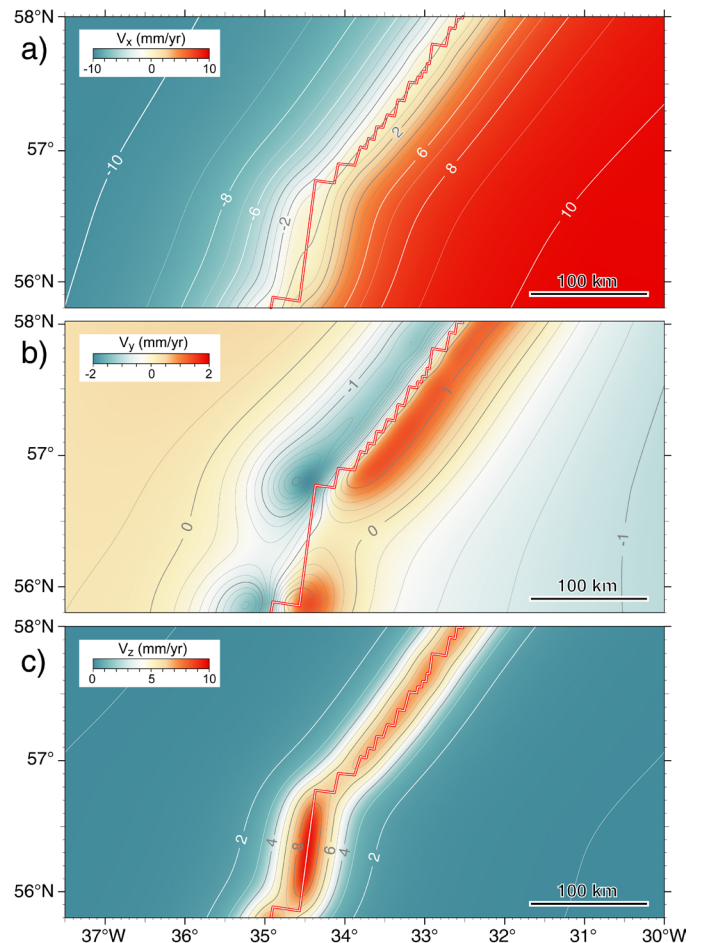

Fig. 7 - Plate thickening passive mantle flow velocities at a depth of 25 km. Assumed spreading rate is 10 mm/yr. Magnitude of: a) E-W velocity component (V_x) contoured at 1 mm/yr; b) N-S component (V_y) contoured at 0.2 mm/yr; and c) vertical component (V_z) contoured at 1 mm/yr.

Table 1 - Dredging site locations and sampled rock lithologies. Pe, peridotites; Du, dunites; Ga, gabbros; Do, dolerites; Ba, basalts; Sed, sediments; Others, organic and allochthonous material.

Dredge	Location	On Bottom			Off Bottom			Lithology (%)							
		Lat	Long	Dep(m)	Lat	Long	Dep(m)	Pe	Du	Ga	Do.	Ba	Sed	Others	Kg
V53-01	Charlie Gibbs FZ	52.509	-31.953	2900	52.505	-31.958	2800	2	-	58	40	-	-	-	5.6
V53-02	Charlie Gibbs FZ	52.245	-31.643	4200	52.239	-31.724	3100	-	-	-	-	-	-	-	X
V53-03	Charlie Gibbs FZ	52.489	-31.689	4480	52.485	-31.694	4400	-	-	-	-	100	-	-	0.07
V53-04	Charlie Gibbs FZ	52.469	-31.643	4350	52.469	-31.607	2860	-	-	-	-	-	-	-	X
V53-05	Charlie Gibbs FZ	52.429	-31.366	2700	52.424	-31.384	2400	-	-	-	100	-	-	-	0.81
V53-06	Charlie Gibbs FZ	52.809	-33.789	1480	52.830	-33.782	1130	-	-	-	-	100	-	-	0.41
V53-07	Charlie Gibbs FZ	52.746	-34.195	3100	52.764	-34.190	2400	95.5	1	3	-	-	-	0.5	247.97
V53-08	North Charlie Gibbs FZ	53.651	-35.306	2740	53.653	-35.313	2700	-	-	-	-	100	-	-	134.1
V53-09	North Charlie Gibbs FZ	53.849	-35.362	2500	53.850	-35.376	2460	-	-	-	-	100	-	-	154.4
V53-10	South Bight FZ	56.169	-34.804	1500	56.162	-34.829	1200	-	-	-	-	83	17	-	104.9
V53-11	South Bight FZ	56.195	-34.414	1980	56.193	-34.429	1860	-	-	-	-	100	-	-	76.1
V53-12	South Bight FZ	56.398	-34.400	2000	56.397	-34.403	1900	-	-	-	-	100	-	-	54.2
V53-13	South Bight FZ	56.409	-34.605	1750	56.412	-34.607	1740	-	-	-	-	100	-	-	153.6
V53-14	South Bight FZ	56.553	-34.483	1780	55.546	-34.516	1150	-	-	-	-	16	84	-	115.2
V53-15	South Bight FZ	56.714	-34.679	1800	56.715	-34.688	1630	-	-	-	9	91	-	-	31
V53-16	Modred NTO	56.859	-34.871	1650	56.869	-34.869	1530	-	-	-	-	100	-	-	11.4
V53-17	Modred NTO	57.064	-34.761	1300	57.079	-34.764	1200	-	-	-	43	57	-	-	0.1
V53-18	Modred NTO	57.089	-34.892	2040	57.103	-34.907	1800	91	-	-	-	9	-	-	11.3
V53-19	NTO-Bight FZ	56.846	-33.952	3000	56.846	-33.952	3000	-	-	-	-	100	-	-	5.2
V53-20	NTO-Bight FZ	56.837	-34.072	3100	56.841	-34.072	3050	-	-	-	-	-	-	-	X
V53-21	Bight FZ	56.752	-34.195	3130	56.758	-34.202	3100	-	-	-	-	-	-	-	X
V53-22	Modred NTO	57.031	-34.398	1400	57.033	-34.400	1300	-	-	-	-	96	4	-	38.4
V53-23	Modred NTO	56.835	-34.385	1430	56.837	-34.387	1440	-	-	-	-	100	-	-	91.4
V53-24	Bight FZ	56.744	-34.224	3100	56.750	-34.224	3050	-	-	-	-	99	1	-	73.5
V53-25	Modred NTO	56.790	-34.207	2460	56.804	-34.209	1770	-	-	-	11	88	-	1	135.5
V53-26	Modred NTO	56.949	-34.002	2060	56.956	-33.990	2000	-	-	-	-	100	-	-	0.1
V53-27	Modred NTO	56.967	-34.133	2000	56.977	-34.137	1500	-	-	-	25	73	2	-	58.8
V53-28	South Bight FZ	56.595	-33.937	1500	56.597	-33.940	1400	-	-	5	1	92	-	2	252.4
V53-29	South Bight FZ	56.673	-33.707	1500	56.673	-33.707	1500	-	-	-	-	-	-	-	0
V53-30	South Bight FZ	56.698	-33.718	1700	56.693	-33.713	1650	3	-	-	-	73	24	-	60.7
V53-31	Modred NTO	56.796	-33.511	1200	56.805	-33.497	900	-	-	-	-	100	-	-	24.6
V53-32	Modred NTO	56.795	-32.952	1150	56.795	-32.952	1150	-	-	-	21	79	-	-	1.1

core V53-C2 was collected from 3138 m water depth at the southern termination of the Gardar Drift (53°03.301'N; 33°32.719'W, Figs.1 and 3). The core is 520 cm long. The coring sites are located below a depth of 1600 m, which represents the upper limit of a component of the North Atlantic Deep Water-Iceland-Scotland Overflow Water; thus, transformation and flow intensity of the North Atlantic Deep Water both influenced the sedimentary processes in the study area in the geological past (e.g., Morozov et al., 2010).

The sediment cores were cut onboard into ~ 90 cm sections and split into two halves (archive and working halves), then photographed and lithologically described including the colour definition from the Munsell Soil Colour Charts. The working halves were continuously sampled with a 1-cm step and packed in airtight bags. The archive halves were packed in plastic pipes one meter in length. The samples were then stored in a cool room (4°C). Subsamples (each 10 cm) were taken using 8 cm^3 plastic cubes for preliminary analysis under the microscope.

RESULTS

Bathymetry and magnetics

Multibeam bathymetry of the two study areas (Bight and Charlie Gibbs) has been described by Hey et al. (2016) and by Skolotnev et al. (2020), respectively. Here, we only report a 100-km long E-W profile acquired with the EA600 echo sounder across the MAR between the Bight transform and the Modred NTO (Fig. 8; profile M-M'). The MAR axis, oriented NNE-SSW, is slightly oblique to the spreading direction. The axial valley is ~ 11 km wide and ~ 20 km long. It is bounded by two main normal faults that lower the valley floor by ~ 1 km (from an average depth of ~ 2000 m up to ~ 3000 m), while an imponent (~ 5 km wide and ~ 500 m high) neo-volcanic zone dominates the central sector of the valley (Fig. 8a). The eastern side of the ridge segment is shallower than the western side. A comparison of the bathymetric profile (blue solid line in Fig. 8b) with the depth-age curve of the North Atlantic Ocean (blue dashed line in Fig. 8b), calculated after Crosby et al. (2006) and assuming a half-spreading rate of 10 mm/yr, shows that the seafloor of the eastern side follows the theoretical subsidence rate, while that of the western side differs strongly, with no/little deepening at increasing crustal age. Magnetic anomalies along the same profile also show a strong asymmetry with respect to the ridge axis, with a central anomaly (c1n) shifted eastward and subdivided into two peaks (Fig. 8c).

Gravity

The calculated Mantle Bouguer anomaly shows a prominent negative circular zone centered on the MAR segment south of the Bight transform (Fig. 6b), consistent with the "bull's eye" MBA pattern detected elsewhere along the MAR (Kuo and Forsyth, 1988; Lin et al., 1990), and reflecting thicker crust and/or hotter mantle at the segment's center. The MBA increases with age of the seafloor due to changes in mantle density induced by cooling of the lithosphere (Fig. 6b). Low MBA anomalies within fracture zones, in particular on the eastern flank of the MAR, may be related to the presence of a thick sedimentary cover not included in the computation.

Topography and mantle Bouguer anomaly along the Reykjanes Ridge axis show an absence of segmentation (Fig. 6). There, the along axis zero-age MBA profile shows little variations (max 10 mGal) around the average value of -60 mGal, whereas larger variations are observed crossing the Modred NTO, the Bight transform and along the MAR southern segment where the MBA anomaly reaches the local minimum value of -65 mGal at the center of the ridge segment (Fig. 6c and d).

Residual anomalies (RMBA), obtained by subtracting the predicted gravity field due to thermal mantle density variations (Fig. 9a) from the mantle Bouguer anomalies
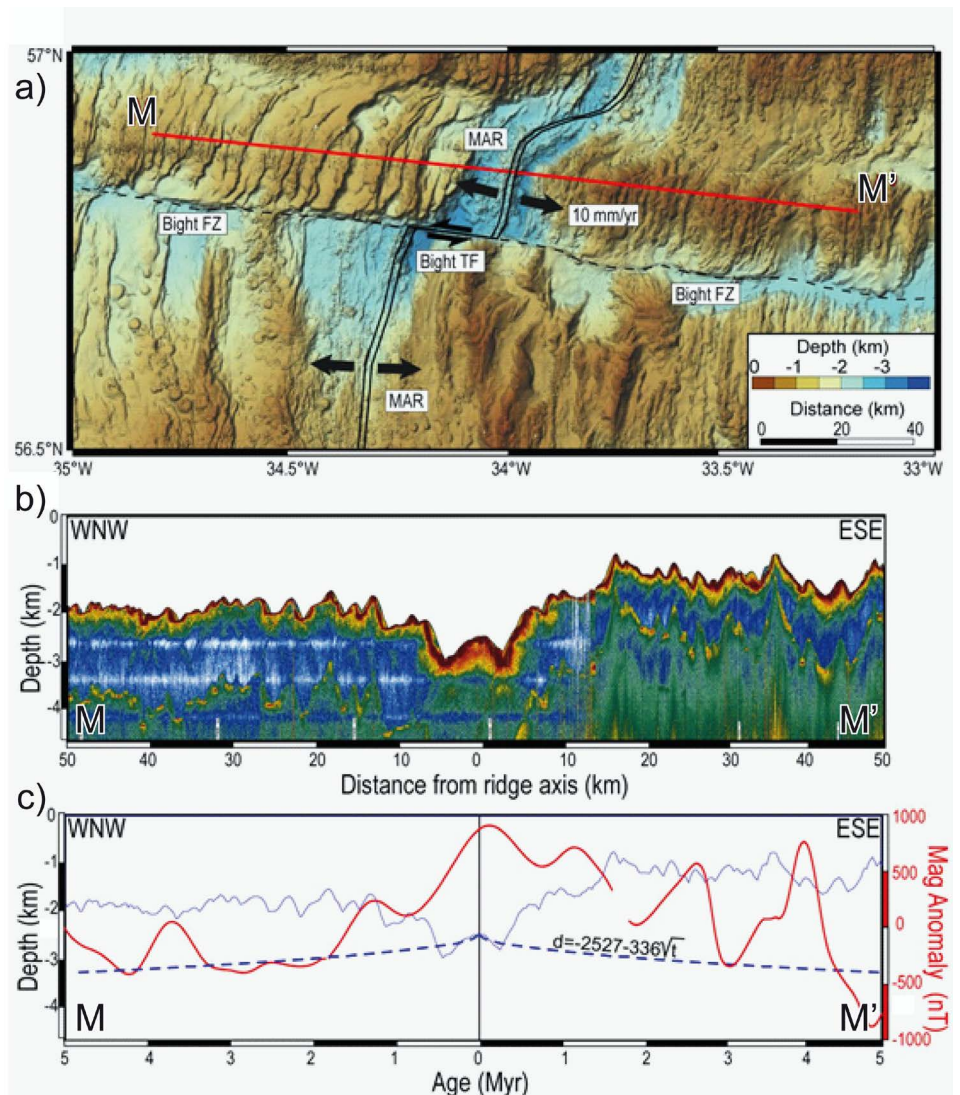

Fig. 8 - a) Bathymetry of the Bight area. Red solid line locates profile M-M' shown in (b) and (c). Double black solid lines: MAR spreading segments; solid line: Bight Transform Fault (TF); dashed line: Bight Fracture Zone (FZ); Arrows: plate motions. b) M-M' bathymetry. Colours indicate reflection strength variations; and c) covariations between depth, theoretical subsidence and magnetic anomalies along profile M-M'. Red and blue solid lines, magnetics and bathymetry, respectively. Blue dashed line, depth-age subsidence curve calculated after Crosby et al. (2006).

(Fig. 6b), were arbitrarily shifted by a constant, assuming the average value as zero level (Fig. 9b). The peak-to-peak variation of RMBA has been reduced from the free air anomaly by ~ 60%. The RMBA local minima, located in correspondence of the MAR segment and of the Reykjanes Ridge, are expected to result from variations in crustal thickness and/or from an incorrect parameterization of the mantle thermal model because dynamic contributions to mantle flow have been neglected. Downward continuation of the RMBA at the depth of 10 km provides an estimate of the variations in crustal thickness (low density layer, LDL) in the Bight transform region (Fig. 9c). Crustal thickness ranges from 4 to 14 km with a thick crust (> 8 km) below the central sector of the MAR segment south of the Bight transform (up to 9 km), the western flank of the Reykjanes axial valley (up to 10 km) and below fracture zones in particular on the eastern side of the MAR (> 11 km; Fig. 9c). A thin crust (< 8 km) is predicted in a 80 km-long 20 km-wide stripe across the northern part of the southern MAR segment next to its intersection with the Bight transform. Here, the thinnest crust (~ 4 km) is found below a serie of smooth structural highs to the east of the ridge axis (Figs. 2 and 9c). A thin crust is also predicted below the oldest sectors of the transverse ridges related to the Bight transform and Modred NTO; and below the V-shaped ridges flanking the Reykjanes Ridge (Fig. 9c).

Lithology

At the Bight Fracture Zone, dredge hauls consist of 88 wt% of pillow basalts and basalt breccia, locally with dolerites (3 wt%) (Fig. 10b). Gabbros (1 wt%) and harzburgites (0.8 wt%) are minor lithologies recovered in 3 dredges deployed on three bathymetric highs (Fig. 2). Rafted continental material was abundantly sampled but not included in the description. Sedimentary rocks (7.2 wt%) were also sampled off-axis (Dredges V53-10 and V53-22).

The new dredge hauls at the Charlie Gibbs FZ confirm the results of Expedition S50 (see Skolotnev et al, 2021; Fig. 10a). Pillow basalts, which represent the main rock-type (54 wt%), were collected in the northern MAR sector and along the ITR segment (Figs. 3 and 11). Dolerite (Fig. 11i) and gabbros (0.7 wt%; Fig. 12) were recovered on corrugated surfaces. Peridotites (44 wt%) and minor rodingitized gabbros (1.3 wt%) were mainly collected along the northern wall of the northern transform valley (Dredge V53-07; Figs. 12 and 13).

Basalts and dolerites

Basalts were distinguished from dolerites based on texture and/or the presence of volcanic glass; dolerites are characterized by a crystalline matrix with subophitic texture and the absence of glass. Basalts commonly display brittle deformation ranging from fractured (grade 1) to brecciated without clast rotation (grade 2) to densely fractured (grade 3).
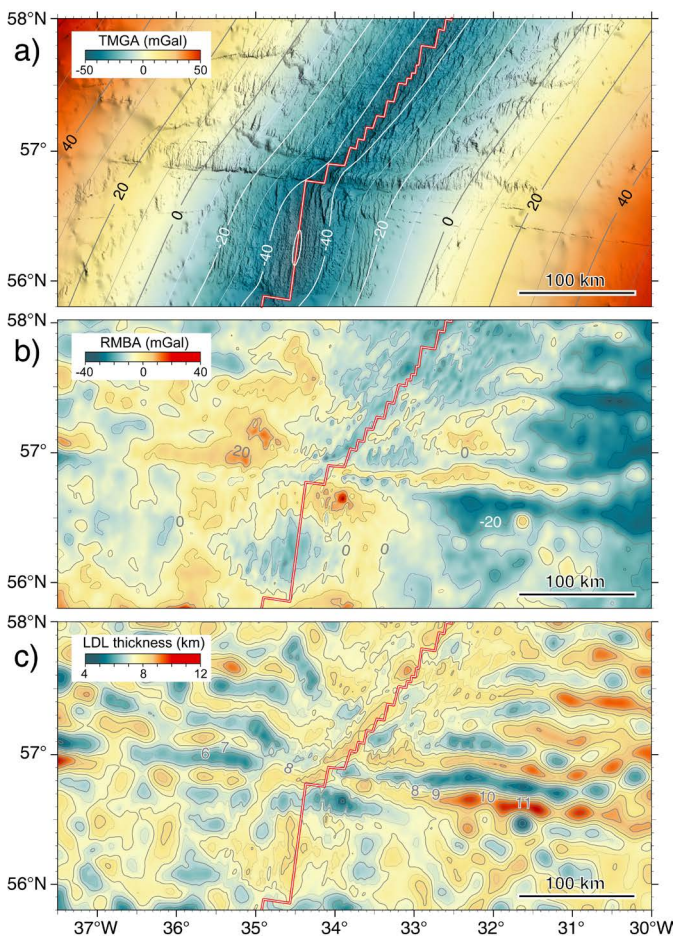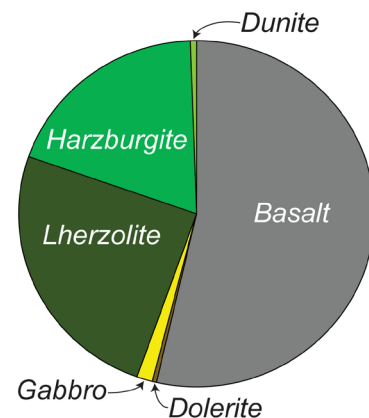

Fig. 9 - Gravity analyses results of the Bight transform region. a) Predicted gravity anomalies (TMGA) due to density variations caused by the computed mantle thermal structure. Shaded background: bathymetry. b) Residual Mantle Bouguer anomaly. **c)** Inferred crustal thickness obtained after downward continuation of the RMBA at a depth of 10 km.
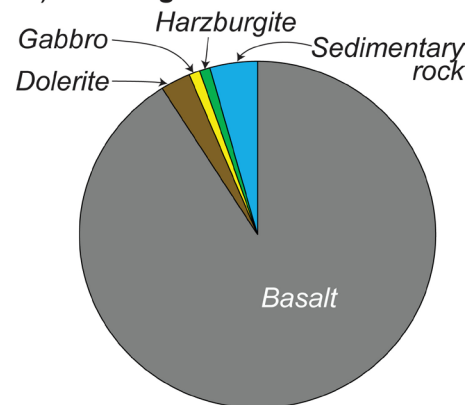

Fig. 10 - Modal proportions (pie diagrams) of the lithologies recovered during V53 at a) Charlie Gibbs and b) Bight Fracture Zones. Each colour represents a different lithology.
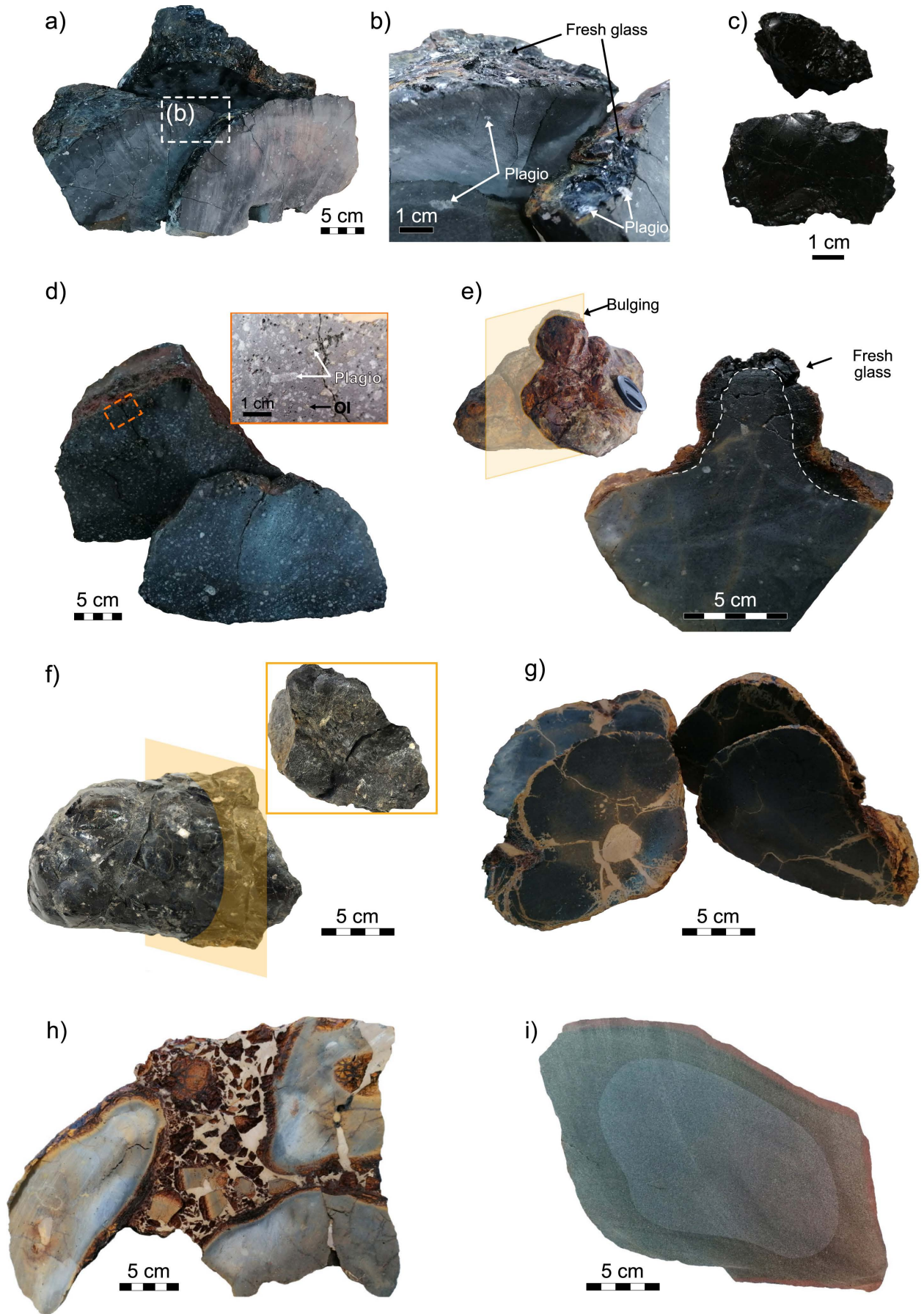
Fig. 11 - Hand-sample photographs of the recovered volcanic lithologies; a) Fresh pillow basalt recovered along the MAR North axis in the vicinity of Charlie Gibbs FZ; b) close-up of the pillow basalt glass rim; c) large glass fragments recovered at the Charlie Gibbs ITR axis; d, e, f) fresh to slightly palagonitized basalts sampled at the Bight FZ; g) highly altered basalt sampled off-axis south of the Bight FZ; h) basaltic monomictic breccia sampled off-axis in volcanic fabric structures at the Bight FZ; i) partially altered dolerite sampled in the Bight FZ.

At the Bight Fracture Zone (Fig. 2), basalts have been recovered along the MAR axis (V53-11, V53-12, V53-24) and on the older volcanic fabric structures, up to ~ 24 km west from the present-day rift axis (V53-10, V53-13, V53-14, V53-15). East of the MAR axis, basalts were sampled on two bathymetric highs (V53-28, V53-30). Between the Bight transform and the Modred NTO, 6 dredges recovered basalts from the present-day ridge axis (V53-19), and up to ~ 70 km away from it to the east (V53-31, V53-32) and to the west (V53-25, V53-23, V53-16; Fig. 2). The dredges deployed on

a)

2 cm

b)

Rodingitized gabbro

2 cm

Serpentinized peridotite

c)

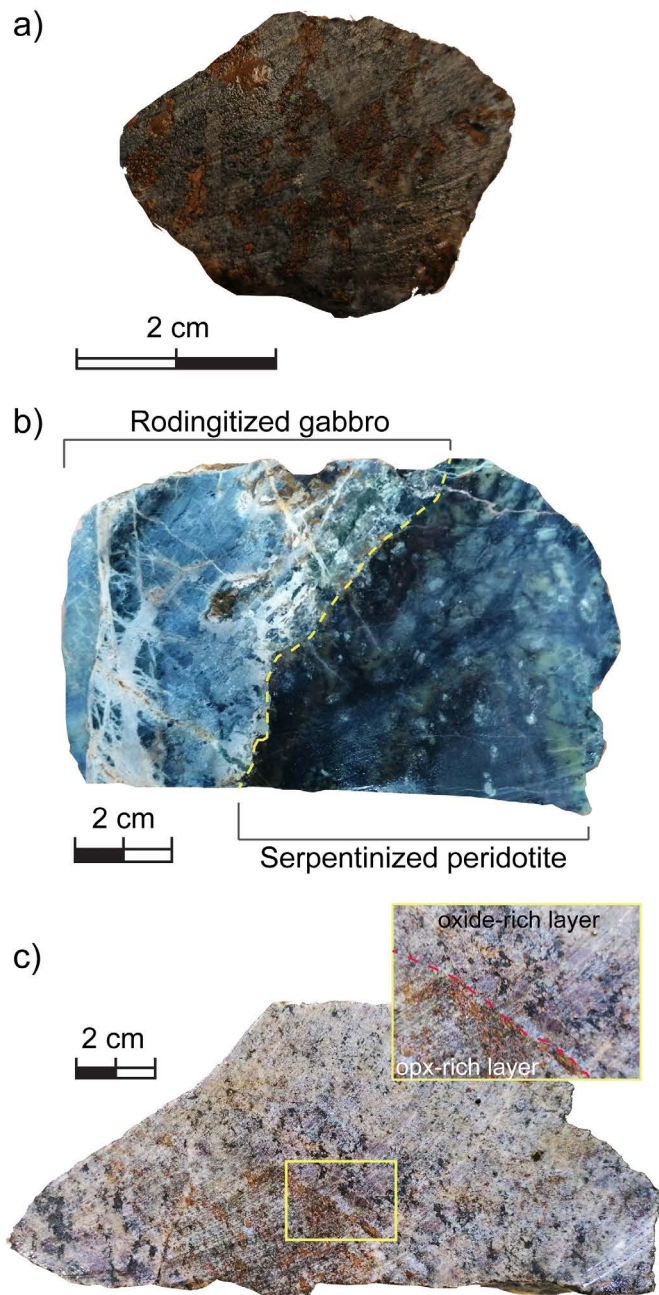oxide-rich layer

opx-rich layer

2 cm

Fig. 12 - Hand-sample photographs of the recovered gabbroic rocks; a) Sub-ophitic gabbro recovered from OCC structures in the Charlie Gibbs ITR Domain; b) Rodingitized gabbro in contact with a serpentinized peridotite sampled from the northern transform wall of the Charlie Gibbs northern transform valley; c) Gabbroic sample showing a diffuse contact between an oxide gabbro layer and a gabbronoritic layer, recovered from an off-axis bathymetric high east from the MAR axis, south of the Bight FZ.

the volcanic fabric structures north of the Modred NTO sampled basalts at increasing distance from the Reykjanes Ridge, up to ~ 65 km to the west (V53-26, V53-27, V53-22, V53-17, V53-18). Fresh to slightly palagonitized basalts were mostly sampled at the ridge axes in the three domains (Fig. 11d, e and f). Nearly intact pillow and tubular basalts with thick unaltered glass rims (from 5 to 30 mm; Fig. 11d, e and f) and textures range from aphyric to phyric, with phenocrysts of olivine and plagioclase (up to 30 vol%) in variable proportions. Overall, the vesicularity is low (< 10%), with rare exceptions showing up to 30%. Altered basalts sampled away from the ridge axes show variable alteration, from moderately to highly altered with fully palagonitized glass and fractures, and vesicles filled with clay (Fig. 11g). Basalt alteration increases with increasing distance from the present-day ridge axes. Basaltic monomictic breccias are ubiquitous away from the ridge axis (Fig. 11h): they are composed of angular to subrounded basaltic clasts, often associated with smaller clasts of partly to fully palagonitized glass, both embayed in a clay matrix (Fig. 11h). Dolerites from the Bight Fracture Zone have been sampled together with basalts exclusively away from the present-day ridge axes (V53-14, V53-15, V53-25, V53-27, V53-17; Fig. 2). They are commonly characterized by a crystalline matrix with ophitic to subophitic texture (Fig. 11i). All dolerite samples are variably altered (Fig. 11i) with partial substitution of the original clinopyroxene by chlorite and of plagioclase by epidote and albite.

At the Charlie Gibbs Fracture Zone (Fig. 3), basalts have been recovered along the MAR North spreading axis (V53-08, V53-09) and on top of a bathymetric high located 70 km east of the MAR North axis, along the northern wall of the northern transform valley (V53-06) (Fig. 3). At the ITR axis, large fragments of fresh glass have been recovered (V53-03) (Fig. 11c). Fresh intact pillow basalts to slightly altered fragments of pillow basalts have been sampled at the MAR North axis (Fig. 11a and b). Fresh pillow basalts show unaltered glass rims (up to 30 mm; Figs 11a and b), whereas basalt fragments show no glass or palagonitized glass rims. Few decimetre-size samples present tubular shapes and thin rims of fresh glass (up to 5 mm). The basalts show textures ranging from phyric, with olivine and plagioclase phenocrysts (up to 8 vol%; Dredge V53-08; Fig. 11a and b), to sparsely phyric (< 5 vol% phenocrysts) and aphyric (0 vol% phenocrysts; Dredge V53-09).

Dolerites from the Charlie Gibbs Fracture Zone have been sampled at the two bathymetric highs located on the eastern and western sides of the ITR axis (V53-01, V53-05). They are characterized by a crystalline matrix with ophitic to subophitic texture. All dolerite samples are variably altered with partial substitution of the original clinopyroxene by chlorite and of plagioclase by epidote and albite.

Gabbros

At the Bight Fracture Zone, a single sample of oxide gabbro has been recovered from a crest-like bathymetric high located ~ 25 km east of the MAR (V53-28; Fig. 2). This gabbro shows a weak magmatic foliation and displays a contact between oxide gabbro and a 5 cm-thick layer of gabbronoritic composition (i.e., occurrence of euhedral orthopyroxene) (Fig. 12c).

At the Charlie Gibbs Transform Zone, gabbros have been recovered from one OCC, west of the Intra-Transform Ridge (V53-01), and along the northern wall of the northern transform valley (V53-07) (Fig. 3). The OCC gabbros show variable degrees of alteration and preserved subophitic magmatic textures (Fig. 12a). They are coarse- to fine-grained gabbros *sensu stricto* (60% plagioclase, 40% clinopyroxene) with no
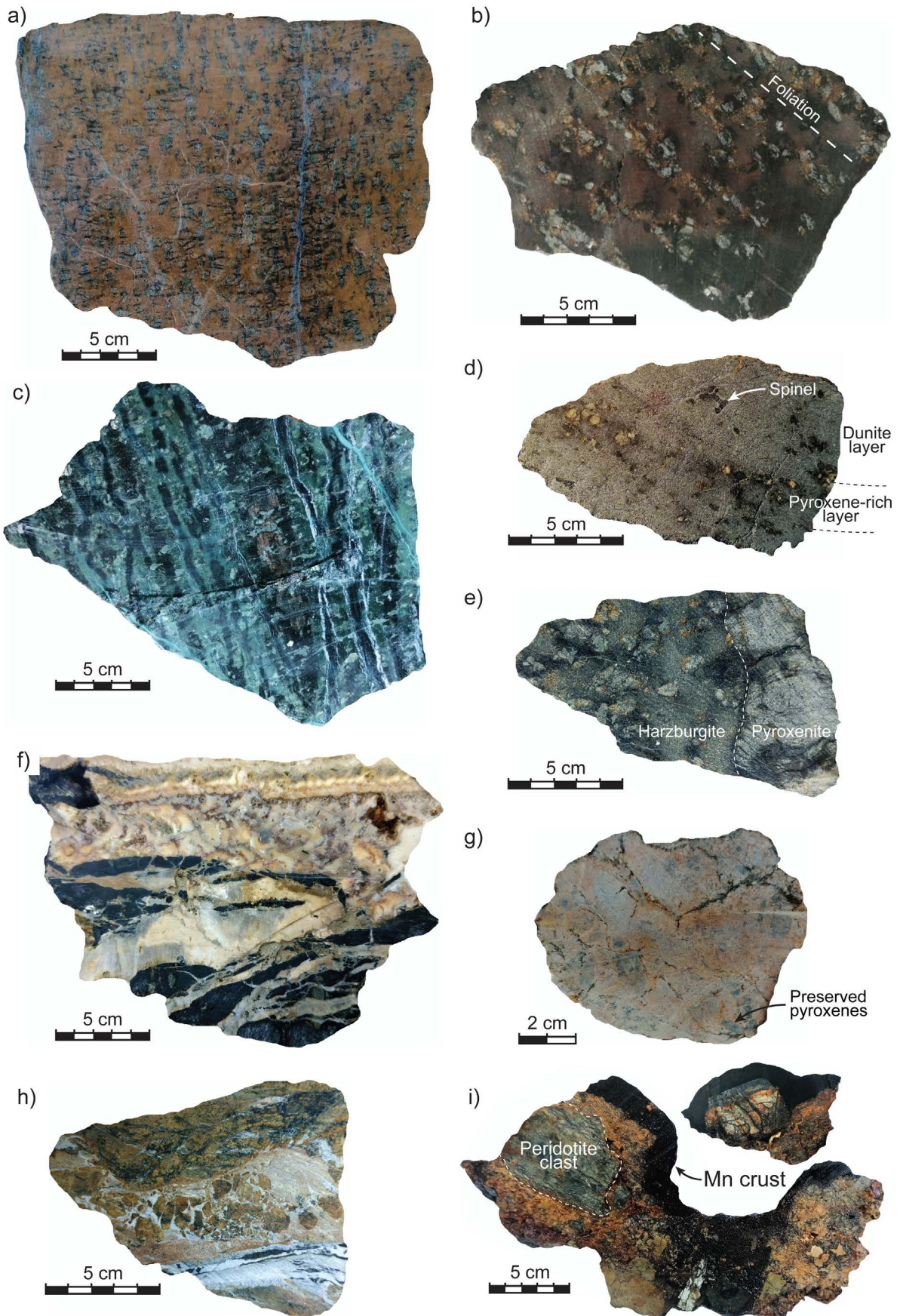
Fig. 13 - Hand-sample photographs of recovered ultramafic rocks recovered from flanks of bathymetric highs and transform walls in the Charlie Gibbs region (a-h), and in the Bight region (i). a) Weakly altered lherzolite; b) Strongly altered harzburgite; c) Fully altered serpentinite; d) Dunite showing the occurrence of a pyroxene-rich layer; e) Weakly altered harzburgite in contact with a preserved pyroxenite layer; f) Fully altered serpentinite crosscut by carbonate- to serpentine-filled veins and fractures; g) listvenite showing the occurrence of few preserved orthopyroxenes; h) cataclastic breccia with oxidized peridotite clasts embedded in a fine-grained matrix cemented by carbonate minerals; i) polymictic breccia showing rounded clasts of serpentinized harzburgite and covered by a centimetre-thick manganese crust.

clear magmatic foliations, unlike the olivine gabbros sampled in similar OCC structures during Expedition S50 at the Charlie Gibbs Transform Zone (Skolotnev et al., 2021). Conversely, the gabbroic rocks from the transform wall are partly transformed into rodingites (Fig. 12b), indicating that the alteration of the gabbros followed the serpentinization of the host peridotites (e.g., Bach et al., 2013; Tamura et al., 2016). Due to contact with harzburgites, some gabbros are converted to an association of sodic plagioclase, low-temperature garnet and tremolite (e.g., Bach and Klein, 2009).

Peridotites

At the Bight Transform Zone, peridotite clasts were found in polymictic breccia (Fig. 13i) dredged on bathymetric highs north and south of the Modred NTO and Bight FZ, respectively (Fig. 2). The clasts are rounded, highly serpentinized and oxidized but display mesh textures, typical of serpentinized peridotites.

At the Charlie Gibbs Transform Zone, peridotites have been recovered from the OCC structure west of the intra-transform ridge segment (V53-01), and along the northern wall of the northern transform valley (V53-07) (Fig. 3). Sampled peridotites range in composition from variably altered lherzolites (> 5 vol% clinopyroxene; Fig. 13a) to harzburgites (< 5 vol% clinopyroxene; Fig. 13b) and minor dunites (> 90 vol% olivine; Fig. 13d). One peridotite sample contains a 3 cm-thick pyroxenite vein composed of large pyroxene and brown spinel (Fig. 13e). Alteration ranges from slightly serpentinized and oxidized, commonly observed in the lherzolites (Fig. 13a), to fully serpentinized. The latter typically shows a dense network of oriented serpentine veins overprinting and crosscutting the primary mineralogical assemblage (Fig. 13c). Additionally, lherzolites show olivines replaced by clay minerals, commonly attributed to superficial weathering. Most samples show carbonate- to serpentine-filled veins and microfractures (Fig. 13f). Few samples of listvenites were recovered (Fig. 13g). Despite alteration, all peridotites show variable degrees of crystal plastic deformation (CPF), ranging from weakly foliated (grade 1) to strongly foliated (grade 2; Fig. 13b). One sample shows strong cataclastic deformation (brittle grade 5)

with oxidized peridotite clasts embedded in a fine-grained matrix cemented by carbonate minerals (Fig. 13h).

Sedimentary rocks

A few sedimentary rocks have been dredged from the volcanic fabric structures away from the present-day ridge axis at the Bight Fracture Zone (Fig. 2), and range in composition from mudstones to sedimentary polymictic breccias including gastropods, bivalves and corals into a fine-grained carbonate matrix (Fig. 14).

Continental drafted blocks and biogenic material

Continental rafted blocks have been recovered ubiquitously at the Bight and Charlie Gibbs Fracture Zones. Their composition span from granitic to gneisses, amphibolites, eclogits, and sandstones. This lithotype has already been reported at the Charlie Gibbs Fracture Zone during Expedition S50 onboard the *R/V A.N. Strakhov* (Skolotnev et al., 2021) and has not been included in the description of the sampled lithologies during Expedition V53 (this study).

Present days corals (Fig. 14b) were found on the surface of samples recovered away from the ridge axis in the Bight region, and curiously, few specimens of abyssal wildlife were trapped in the dredges during recovery.

Sedimentary cores

The V53-C1 sedimentary section shows downcore coarsening and increase in density, as well as a mottled texture indicative of bioturbation (Fig. 15). Only the 3.58-3.76 m interval is characterized by a straight layered texture. The sediments mainly display different shades of grey and brown, with smooth and gradual contacts between the layers (Fig. 15). The upper part of the core (0-0.46 m) is composed of heavily watered silty-clayed mud, which is replaced by clays and silty clays in the lower interval (0.46-2.8 m), while the bottom section (2.8-4.65 m) is mainly composed of sandy clays. The 3.3-3.75 m and 2.2-2.75 m intervals are formed by sediments with poorly preserved calcareous foraminifera. At the 3.75, 3.91, 4.15, and 4.31 m horizons, we found single inclusions of gravel-sized granitic rocks.
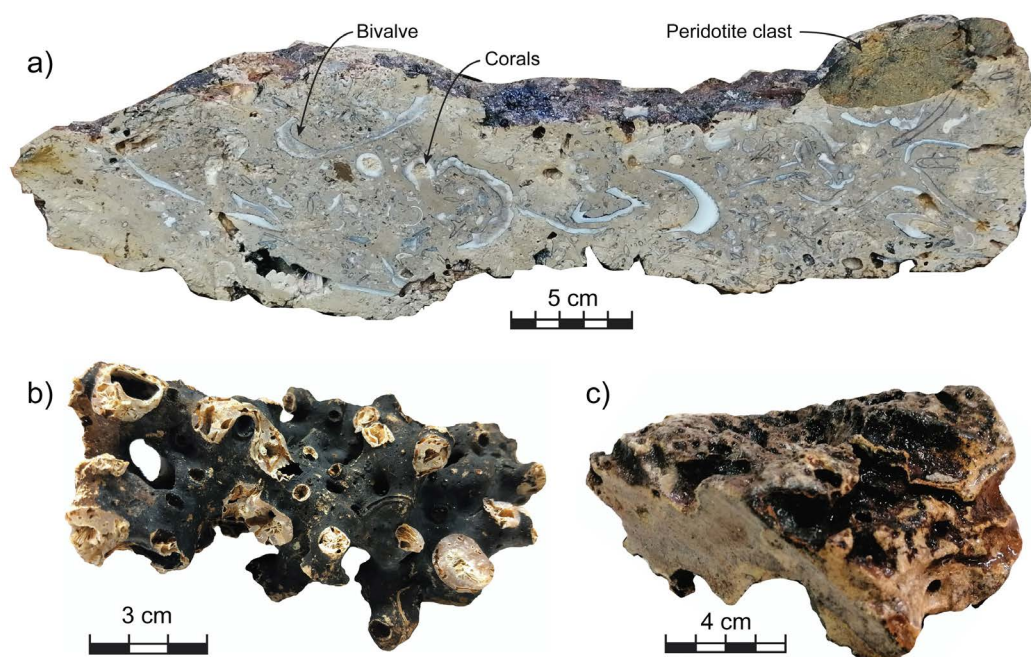
Fig. 14 - Hand-sample photographs of the recovered sedimentary rocks and biogenic material. a) Polymictic breccia including gastropods, bivalves and corals into a fine-grained carbonate matrix; b) Present-day corals; c) Polymictic breccia showing traces of bioturbation.
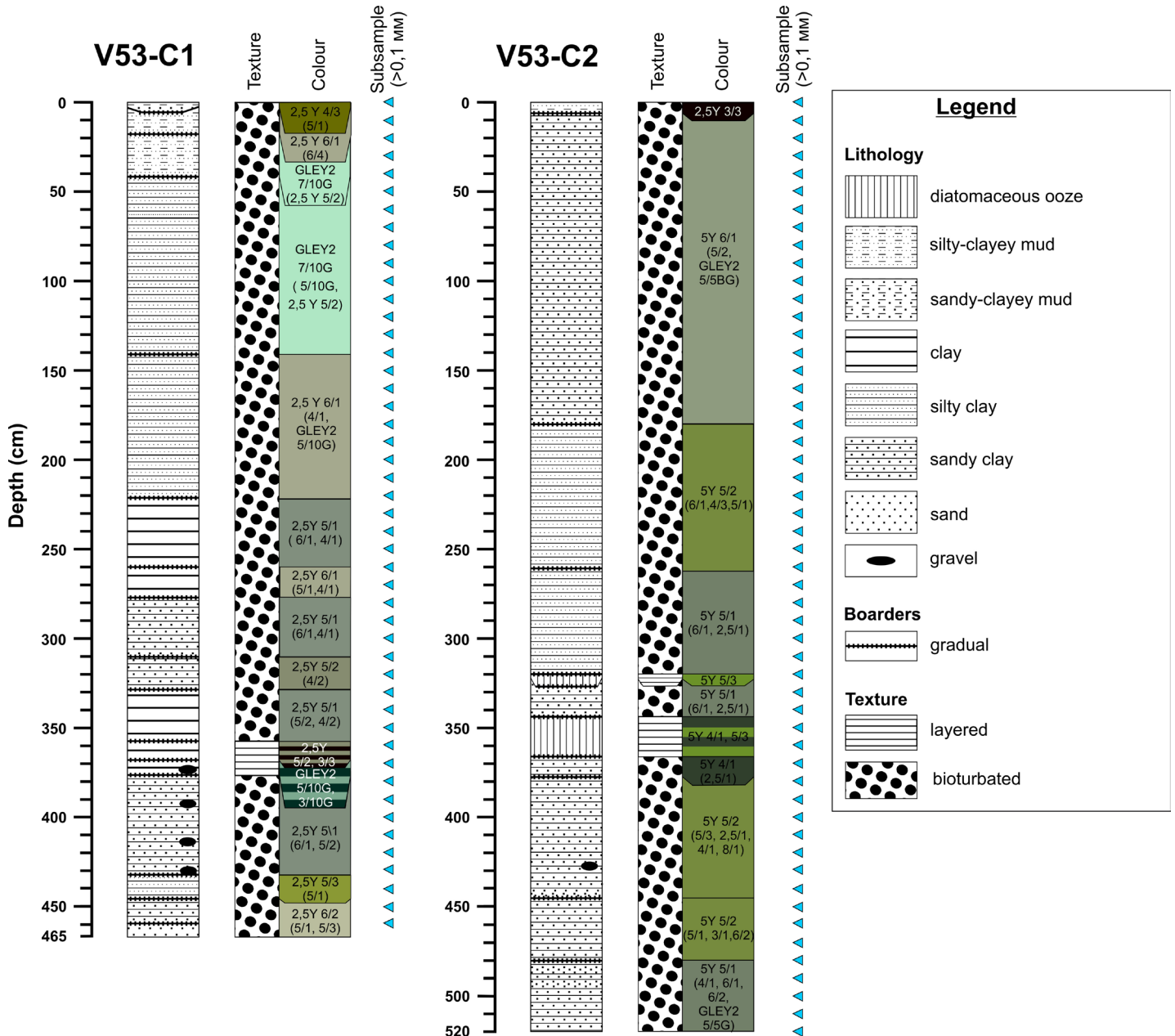
Fig. 15 - Lithological description of the sedimentary gravity cores V53-C1 and V53-C2 recovered at the Charlie Gibbs FZ. Detail of the texture, colour and location of subsampling is represented in the right column for both cores.

Core V53-C2 is characterized by a mottled texture, indicative of bioturbation, and distinct burrows, apart from the 3.20-3.21 m and 3.41-3.66 m intervals consisting of very fine micro-layered sediments (diatom ooze). The sediments show various shades of grey and olive (Fig. 15), with gradual contacts between the layers. The core is mainly composed of silty and sandy clays. The 3.2-3.66 m interval consists of poorly sorted sediments with numerous organic remains (scales, fish bones). A single gravel was found at the 4.27-4.28 m horizon.

In both cores, the coarse fraction of the upper part is mainly represented by carbonates, while in the bottom sections the proportion of terrigenous material increases. It is worth noting the presence of volcanic glass in the sandy layers of both cores.

DISCUSSION

Recent variations in seafloor accretion at the Bight Fracture Zone

In recent geological times, the ridge geometry drastically changed on both sides of the Bight Fracture Zone, under the growing influence of the Icelandic plume (Benediktsdóttir et al., 2016). The progressive southward propagation of the Reykjanes Ridge caused an abrupt variation from a highly segmented ridge to an overall continuous ridge axis striking oblique to the spreading direction. Previous analyses localized the tip of the propagator between the Modred NTO and the Bight transform (Hey et al., 2016; Martinez and Hey, 2022). Consistently, the current accretionary style

of the Reykjanes Ridge north of the Modred NTO is fully magmatic, as evidenced by a thick crust below the ridge axis (Fig. 9c), a basaltic seafloor with a well-developed volcanic fabric carpeting both flanks of the ridge (Fig. 2), and numerous low-intensity earthquakes along-axis, linked to normal faulting (Fig. 4). Seafloor generated by the short ridge segment between the Modred NTO and Bight transform shows regular volcanic fabrics up to 150 km from the ridge axis, indicating a fully magmatic spreading style for several million years (~ 15 Ma). However, gravity inversion predicts a thinner crust in terrains older than ~ 6 My (Fig. 9c), suggesting a recent increase in melt production at the ridge segment.

During Expedition V53, we sampled a few basement rocks (peridotites and gabbros) on bathymetric highs located north and south of the Modred NTO and Bight Fracture Zone, respectively (Dredges V53-18, V53-28 and V53-30; Fig. 2). These bathymetric highs are presently located 80 km to the west and 35 km to the east of the present-day ridge axis. Gravity inferred crustal thickness suggests a thin crust under their flanks (Fig. 9c), with exhumation of deep material at the footwalls of normal faults. Assuming the present-day plate boundary geometry and a spreading rate of 10 mm/yr, the age of these structures can be constrained at approximately 8 and 3.5 My, respectively. The Mid-Atlantic Ridge segment south of the Bight transform is known to have been relocated ~1 My about 15 km toward the east (Benediktsdóttir et al., 2016). Therefore, the bathymetric highs south of the Bight Fracture Zone must have been at further distance (~ 60 km) from the active rift axis before the ridge jump, and their age can be estimated to be older than ~ 6 My. The exact nature of these bathymetric highs cannot be defined from the preliminary data. However, the occurrence of dome-like structures suggests that the basement rocks might have been exposed by long-lived detachment faults predating the impingement of the Iceland propagator, north of the Bight transform. Consequently, before being crosscut by the propagating Reykjanes Ridge, the seafloor accretion style must have been drastically different and characterized, at least locally, by tectonic spreading associated with the exhumation of deep-seated material through detachment faulting, similar to several segments along the central portions of the Mid-Atlantic Ridge (Escartin et al., 2008; Dick et al., 2008; Smith et al., 2014; Sanfilippo et al., 2018).

Long-lived tectonic accretion at the Charlie Gibbs intra-transform domain

The Charlie Gibbs transform is characterized by two transform faults that displace the Mid-Atlantic Ridge of ~ 340 km. The two MAR segments are mostly characterized by a well-developed volcanic seafloor, indicative of magmatic accretion. Bathymetric highs exposing peridotites and gabbros suggest a slight decrease in magmatism approaching the Charlie Gibbs transform system from the Northern MAR segment. Conversely, the ITR domain is characterized by a continuous succession of bathymetric highs exposing corrugated surfaces (Fig. 3). Six of these bathymetric highs, located on both flanks of the ITR domains, have been sampled during Expedition S50 and V53 by dredging, and recovered basement material, including mantle peridotites. A preliminary interpretation of these structures suggests that they are OCCs, formed cyclically at the ridge axis, through a process of tectonic crustal accretion persisting at least for 15 Ma, since the furthest OCC identified in the ITR domain

is located 150 km east of the present-day axis. The opposite vergence of some of the detachment surfaces let suppose an asymmetric spreading, dominated by detachment faulting in both directions. A similar accretionary style was proposed for the eastern part of the Southwest Indian Ridge, west of the Rodriguez triple junction: there, plate divergence has been interpreted from seafloor observation and magnetic data to be mainly accommodated by a succession of cross-cutting detachment faults with opposite vergences, exposing mantle-derived rocks on the seafloor (Sauter et al., 2013; Cannat et al. 2019).

CONCLUSIONS

Our preliminary results from expedition V53 of the *R/V A.S. Vavilov* in the North Atlantic suggest different patterns of crustal accretion between the Reykjanes Ridge and the northern Mid-Atlantic Ridge. At mid-ocean ridges, zero-age large-amplitude variations in topography along-axis, mantle Bouguer anomalies together with large magnitude earthquakes and high seismicity, are mostly due to segmentation, suggesting that mantle dynamics give rise to segmentation at slow spreading rates only. Recently, Martinez and Hey (2022) proposed that the different mantle melting pattern below mid-ocean ridges could determine the chemical and rheological structure of the residual mantle, either favouring or inhibiting transform fault formation.

Seafloor morphology, seismicity, MBA and crustal thickness variations at the ridge segments that approach the Bight transform indicate a high magma supply and a thick crust. However, the Reykjanes Ridge north of the Bight transform has no transform faults, while to the south, the MAR shows a typical slow-spreading ridge segment with a thick crust at segment centres and a thin crust at segment ends. This suggests that at hot slow spreading ridges, such as those reported here, the thermal and compositional state of the lithosphere, i.e. its rheology controls ridge segmentation rather than mantle dynamics (Bell and Buck, 1992; Martinez and Hey, 2022).

ACKNOWLEDGMENTS

REFERENCES

Aderhold K. and Abercrombie R.E., 2016. The 2015 Mw 7.1 earthquake on the Charlie-Gibbs transform fault: Repeating earthquakes and multimodal slip on a slow oceanic transform, Geophys. Res. Lett., 43: 6119-6128.

Bach W. and Klein F., 2009. The petrology of seafloor rodingites: insights from geochemical reaction path modeling. Lithos, 112, 103-117.

Bach W., Jöns N. and Klein F., 2013. Metasomatism within the ocean crust. In: Harlov. D.E. and Austrheim, H. (Eds.), Metasomatism and the chemical transformation of rock. Lecture Notes in Earth System Sciences. Springer, Berlin, Heidelberg. https://doi.org/10.1007/978-3-642-28394-9_8.

Benediktsdóttir Á., Hey R., Martinez F. and Höskuldsson Á., 2012. Detailed tectonic evolution of the Reykjanes Ridge during the past 15 Ma. Geochem. Geophys. Geosyst., 13, Q02008, doi:10.1029/2011GC003948.

Benediktsdóttir Á., Hey R., Martinez F. and Höskuldsson Á., 2016. A new kinematic model of the Mid-Atlantic Ridge between 55°55'N and the Bight Transform Fault for the past 6 Ma. J. Geophys. Res. Solid Earth, 121: 455-468, doi:10.1002/2015JB012504.

Bell R.E. and Buck W.R., 1992. Crustal control of ridge segmentation inferred from observations of the Reykjanes Ridge. Nature, 357: 583-586.

Bergman E.A. and Solomon S.C., 1988. Transform fault earthquakes in the North Atlantic: Source mechanisms and depth of faulting, J. Geophys. Res., 93: 9027-9057.

Blichert-Toft J., Agranier A., Andres M., Kingsley R., Schilling J.-G. and Albarède F., 2005. Geochemical segmentation of the Mid-Atlantic Ridge north of Iceland and ridge-hot spot interaction in the North Atlantic. Geochem. Geophys. Geosyst., 6, Q01E19, doi:10.1029/2004GC000788.

Bonatti E., Ligi M., Carrara G., Gasperini L., Turko N., Perfiliev A., Peyve A.A. and Sciuto P.F., 1996. Diffuse impact of the Mid Atlantic Ridge with the Romanche transform: a Ultracold Ridge/Transform Intersection. J. Geophys. Res., 101: 8043-8054.

Bruguier N., Minshull T. and Brozena J., 2003. Morphology and tectonics of the Mid-Atlantic Ridge, 7°-12° S. J. Geophys. Res., 108 (B2), 2093, doi:10.1029/2001JB001172.

Calvert A.J. and Whitmarsh R.B., 1986. The structure of the Charlie-Gibbs Fracture Zone. J. Geol. Soc. London, 143: 819-821.

Cannat M., Sauter D., Mendel V., Ruellan E., Okino K., Escartín J., Combier V. and Baala M., 2006. Modes of seafloor generation at a melt-poor ultraslow-spreading ridge. Geology, 34: 605-608.

Chernysheva E.A. and Kharin G.S., 2009. Magmatic rocks in the Charlie–Gibbs Fracture Zone, North Atlantic Ocean. Petrology, 17: 476-487.

Crosby A.G., McKenzie D. and Sclater J.G., 2006. The relationship between depth, age and gravity in the oceans. Geophys. J. Int., 166 (2): 553-573.

Dick H.J.B., Tivey M.A. and Tucholke B.E., 2008. Plutonic foundation of a slow-spreading ridge segment: Oceanic core complex at Kane Megamullion, 23°30'N, 45°20'W, Geochem. Geophys. Geosyst., 9, Q05014, doi:10.1029/2007GC001645.

Escartìn J., Smith D.K., Cann J., Schouten H., Langmuir C.H. and Escrig S., 2008. Central role of detachment faults in accretion of slow-spreading oceanic lithosphere. Nature, 455: 790-794.

Fleming H.S., Cherkis N.Z. and Heirtzler J.R., 1970. The Gibbs Fracture Zone: a double fracture zone at 52°30'N in the Atlantic Ocean. Mar. Geophys. Res., 1: 37-45.

Furey, T., 2020. Atlantic Ocean Research Alliance (AORA) Bathymetry Data Marine Institute, Ireland.

Georgiopoulou A. and CE18008 Scientific Party, 2018. Tectonic ocean spreading at the Charlie-.Gibbs Fracture Zone (TOSCA): CE18008 Res. Survey Rep., Marine Inst. of Ireland, Dublin, pp 1-24.

Georgiopoulou A. and Murton B., 2018. White paper for the exploration of the Charlie-Gibbs Fracture Zone, central Atlantic. In: Summary Report for the Atlantic Seafloor Partnership for Integrated Research and Exploration Science Planning Workshop, November 15-16, Silver Spring, MD, p. 53-54.

Haworth R.T., 1977. The continental crust northeast of Newfoundland and its ancestral relationship to the Charlie Fracture Zone. Nature, 266: 246-249.

Hekinian R. and Aumento F., 1973. Rocks from the Gibbs Fracture Zone and Minia Seamount near 53°N in the Atlantic Ocean, Mar. Geol., 14: 47-72.

Hey R., Martinez F., Höskuldsson Á. and Benediktsdóttir Á., 2010. Propagating rift model for the V-shaped ridges south of Iceland. Geochem. Geophys. Geosyst., 11, Q03011, doi:10.1029/2009GC002865.

Hey R., Martinez F., Höskuldsson Á., Eason D.E., Sleeper J., Thordarson S., Benediktsdóttir Á. and Merkuryev S., 2016. Multibeam investigation of the active North Atlantic plate boundary reorganization tip. Earth Planet. Sci. Lett., 435: 115-123.

Jones S., 2003. Test of a ridge-plume interaction model using oceanic crustal structure around Iceland. Earth Planet. Sci. Lett., 208 (1-2): 205-218.

Johnson G.L., 1967. North Atlantic fracture zones near 53°N, Earth Planet. Sci. Lett., 2: 445-448.

Johnson G.L., Vogt P.R. and Schneider E.D., 1971. Morphology of the northeastern Atlantic and Labrador Sea. Deutsche Hydrogr. Zeitschrift., 24: 49-73.

Kanamori H., and G.S. Stewart, 1976. Mode of the strain release along the Gibbs Fracture Zone, Mid-Atlantic Ridge. Phys. Earth Planet. Inter., 11: 312-332.

Klein E.M. and Langmuir C.H., 1987. Global correlations of ocean ridge basalt chemistry with axial depth and crustal thickness. J. Geophys. Res., 92: 8089-8115.

Kuo B.-Y. and Forsyth D.W., 1988. Gravity anomalies of the ridge-transform system in the South Atlantic between 31 and 34.5°S: upwelling centers and variations in crustal thickness. Mar. Geophys. Res., 10 . 205-232.

Ligi M., Bonatti E., Cipriani A. and Ottolini L., 2005. Water-rich basalts at mid-ocean-ridge cold spots Nature, 434, 66-69.

Ligi M., Bonatti E., Gasperini L. and Poliakov A.N.B., 2002. Oceanic broad multifault transform plate boundaries. Geology, 30: 11-14.

Ligi M., and Bortoluzzi G., 1989. PLOTMAP: geophysical and geological applications of good standard quality cartographic. Comput. Geosci., 15: 519-585.

Ligi M., Cuffaro M., Chierici F. and Calafato A., 2008. Three-dimensional passive mantle flow beneath mid-ocean ridges: an analytical approach. Geophys. J. Int., 175: 783-805.

Ligi M., Cuffaro M., Muccini F. and Bonatti E., 2022. Generation and Evolution of the Oceanic Lithosphere in the North Atlantic. La Rivista del Nuovo Cimento, 45(7), 460-533.

Lin J., Purdy G.M., Schouten H., Sempere J.-C. and Zervas C., 1990. Evidence from gravity data for focused magmatic accretion along the Mid-Atlantic Ridge. Nature, 344: 627-632.

Lonsdale P. and Shor A., 1979. The oblique intersection of the Mid-Atlantic Ridge with Charlie-Gibbs transform fault. Tectonophysics, 54: 195-209.

MacLeod C.J., Searle R.C., Murton B.J., Casey J.F., Mallows C., Unsworth S.C., Achenbach K.L., and Harris M., 2009. Life cycle of oceanic core complexes, Earth Planet. Sci. Lett., 287: 333-344.

Martinez F. and Hey R., 2022. Mantle melting, lithospheric strength and transform fault stability: Insights from the North Atlantic. Earth Planet. Sci. Lett., 579: 117351, doi:10.1016/j.epsl.2021.117351.

Martinez F., Hey R. and Höskuldsson A., 2020. Reykjanes Ridge evolution: Effects of plate kinematics, small-scale upper mantle convection and a regional mantle gradient. Earth-Sci. Rev., 206, 102956, doi:10.1016/j.earscirev.2019.102956.

Morgan J.P. and Forsyth D.W., 1988. Three-dimensional flow and temperature perturbations due to a transform offset: Effects on oceanic crustal and upper mantle structure. J. Geophys. Res., 93: 2955-2966.

Morozov E.G., Demidov A.N., Tarakanov R.Y. and Zenk W., 2010. Abyssal channels in the Atlantic Ocean. Dordrecht, Heidelberg, London, New York: Springer, pp. 288, doi:10.1007/978-90-481-9358-5

Müller R. and Roest W., 1992. Fracture zones in the North Atlantic from combined Geosat and Seasat data, J. Geophys. Res., 97 (B3): 3337-3350.

Olive J.-A., Behn M.D. and Tucholke B.E., 2010. The structure of oceanic core complexes controlled by the depth distribution of magma emplacement. Nat. Geosc., 3 (7: 491-495.

Olivet J.-L., Le Pichon X., Monti S. and Sichler R., 1974. Charlie-Gibbs Fracture Zone, J. Geophys. Res., 79: 2059-2072.

Olivet J.-L., Sichler B., Thonon P., Le Pichon X., Martinais J. and Pautot G., 1970. La faille transformante Gibbs entre le Rift et la marge du Labrador, C.R. Acad. Sci., Paris, 271: 949-952.

Prince R.A. and Forsyth D.W., 1988. Horizontal extent of anomalously thin crust near the Vema Fracture Zone from the three-dimensional analysis of gravity anomalies. J. Geophys. Res., 93: 8051-8063.

Roberts D.G., Montadert. L. and Searle. R.C., 1979. The western Rockall Plateau: stratigraphy and structural evolution, In: L. Montadert and D.G. Roberts (Eds.), Initial Rep. D.S.D.P., 4X: 1061-1088.

Sandwell D.T., Müller R.D., Smith W.H.F., Garcia E. and Francis R., 2014. New global marine gravity model from CryoSat-2 and Jason-1 reveals buried tectonic structure: Science, 346: 65-67.

Sauter, D., Cannat, M., Rouméjon, S. et al. Continuous exhumation of mantle-derived rocks at the Southwest Indian Ridge for 11 million years. Nature Geosci. 6, 314-320 (2013). https://doi.org/10.1038/ngeo1771

Sanfilippo A., Dick H.J.B., Marschall H., Lissenmeberg J. and Urann B., 2018. Emplacement and high-temperature evolution of gabbros of the 16.5 ºN oceanic core complexes (Mid-Atlantic Ridge): insights into the compositional variability of the lower oceanic crust. Geochem. Geophys. Geosyst., 20: 46-66.

Schilling J.-G., Zajac M., Evans R., Johnston T., White W., Devine J.D. and Kingsley R., 1993. Petrologic and geochemical variations along the Mid-Atlantic Ridge from 29°N to 73°N. Am. J. Sci., 283: 510-586.

Schouten H., Smith D.K., Cann J.R. and Escartín J., 2010. Tectonic versus magmatic extension in the presence of core complexes at slow-spreading ridges from a visualization of faulted seafloor topography. Geology, 38: 615-618.

Searle R., 1981. The active part of Charlie-Gibbs Fracture Zone: a study using sonar and other geophysical techniques, J. Geophys. Res., 86: 243-262.

Sigurdsson H., 1981. First-order major element variation in basalt glasses from the Mid-Atlantic Ridge: 29°N to 73°N. J. Geophys. Res., 86: 9483-9502.

Skolotnev S.G., Sanfilippo A., Peyve A.A., Muccini F., Sokolov S.Y., Sani C., Dobroliubova K.O., Ferrando C., Chamov N.P., Palmiotto C., Pertsev A.N., Bonatti E., Cuffaro M., Gryaznova A.C., Sholukhov K.N., Bich A.S. and Ligi M., 2020. Largescale structure of the Doldrums multi-fault transform system 7-8°N Equatorial Atlantic): preliminary results from the 45th expedition of the R/V A.N. Strakhov. Ofioliti, 45: 25-41.

Skolotnev S.G., Peyve A.A., Sanfilippo A., Ivanenko A.N., Ligi M., Veklich I.A., Petracchini L., Ponomarenko E.P., Basch V., Kuleshov D.A., Ferrando C., Dobrolyubov V.N., Sani C., Shkittin N.A., Bickert M., Dokashenko S.A., Muccini F., Yakovenko E.S., Palmiotto C., Pugacheva T.L. and Cuffaro M., 2022. Peculiarities of the tectonomagmatic processes in the interaction area between the Icelandic Plume and the Bight Transform Fault (North Atlantic). Dokl. Earth Sci., 504: 233-239.

Skolotnev S.G., Sanfilippo A., Peyve A.A., Nestola Y., Sokolov S.Yu., Petracchini L., Dobrolybova K.O., Basch V., Pertsev A.N., Ferrando C., Ivanenko A.N., Sani C., Razumovskii A.A., Muccini F., Bich A.S., Palmiotto C., Brusilovsky Y.V., Bonatti E., Sholukhov K.N., Cuffaro M., Veklich I.A., Dobrolybov V.N. and Ligi M., 2021. Seafloor spreading and tectonics at the Charlie Gibbs Transform System (52-53ºN, Mid Atlantic Ridge): Preliminary results from R/V AN Strakhov Expedition S50. Ofioliti, 46: 83-101.

Smith D, Schouten H., Dick H.J.B., Cann J., Salters V., Marschall H., Sanfilippo A., Ji F., Zheleznov A., Parnell-Turner R., Bai H., Junkin W., Urann B., Curry S., Sulanowska M. and Dick S., 2014. Development and evolution of detachment faulting along 50 km of the Mid-Atlantic Ridge near 16.5°N. Geochem. Geophys. Geosyst., 1: 4692-4711.

Smoot N.C. and Sharman G.F., 1985. Charlie-Gibbs: A fracture zone ridge. Tectonophysics, 116: 137-142.

Sun S.-S. and McDonough W.F., 1989. Chemical and isotopic systematics of oceanic basalts: implications for mantle composition and processes. In: A.D. Saunders and M.J. Norry (Eds), Magmatism in the ocean basins, Geol. Soc. London Spec. Publ., 42: 313-345.

Tamura A., Morishita T., Ishimaru S., Hara K., Sanfilippo A. and Arai S., 2016. Compositional variations in spinel-hosted pargasite inclusions in the olivine-rich rock from the oceanic crust-mantle boundary zone. Contrib. Miner. Petrol., 171 (5): 1-14.

Tucholke B.E., Behn M.D., Buck R. and Lin J., 2008. The role of melt supply in detachment faulting and the formation of oceanic core complexes. Geology, 36 (6), 455-458.

Vogt P.R., 1971. Astenosphere motion recorded by the ocean floor south of Iceland. Earth Planet. Sci. Lett., 13: 153-160.

Vogt P.R. and Avery O.E., 1974. Detailed magnetic surveys in the Northeast Atlantic and Labrador Sea. J. Geophys. Res., 79: 363-389.

Wessel P. and Smith W.H.F., 2006. New, improved version of Generic Mapping Tools released. AGU Eos Trans., 79: 579.

White R.S., 1997. Rift-plume interaction in the North Atlantic. Royal Soc. London Phil. Tr. A, 355: 319-339.

Whitmarsh R.B. and Calvert A.J., 1986. Crustal structure of Atlantic fracture zones - I. The Charlie-Gibbs Fracture Zone. Geophys. J. R. Astr. Soc., 85: 107-138.